**NASA
Technical
Paper
3241**

1993

Analytical and Experimental Investigation of Flutter Suppression by Piezoelectric Actuation

Jennifer Heeg
Langley Research Center
Hampton, Virginia

Contents

Abstract

The objective of this research was to analytically and experimentally study the capabilities of piezoelectric plate actuators for suppressing flutter. Piezoelectric materials are characterized by their ability to produce voltage when subjected to a mechanical strain. The converse piezoelectric effect can be utilized to actuate a structure by applying a voltage. For this investigation, a two-degree-of-freedom wind tunnel model was designed, analyzed, and tested. The model consisted of a rigid wing and a flexible mount system that permitted a translational and a rotational degree of freedom. The model was designed such that flutter was encountered within the testing envelope of the wind tunnel. Actuators made of piezoelectric material were affixed to leaf springs of the mount system. Command signals, applied to the piezoelectric actuators, exerted control over the damping and stiffness properties. A mathematical aeroservoelastic model was constructed by using finite element methods, laminated plate theory, and aeroelastic analysis tools. Plant characteristics were determined from this model and verified by open loop experimental tests. A flutter suppression control law was designed and implemented on a digital control computer. Closed loop flutter testing was conducted. The experimental results represent the first time that adaptive materials have been used to actively suppress flutter. They demonstrate that small, carefully placed actuating plates can be used effectively to control aeroelastic response.

Introduction

Flutter, an interaction between the structural dynamics and the aerodynamics that results in divergent and destructive oscillations of motion, has been observed and documented on aircraft since the era of controlled flight began (ref. 1). Historically, passive solutions such as increasing structural stiffness, mass balancing, or modifying geometry have been used to prevent this hazardous phenomenon. These approaches result in increased weight and cost, and decreased performance. During the past 20 years, there has been considerable research to develop active flutter suppression concepts that use conventional leading and trailing edge aerodynamic control surfaces (refs. 1–5). An active control approach eliminates most of the weight and performance penalties associated with the passive approach and additionally provides a flexibility so that the control law can vary with configuration or flight condition. Active flutter suppression is not a common practice in today's commercial or military aircraft because of several concerns. Flutter is generally of a catastrophic nature; therefore a failure of the system could affect flight safety. As a result, system redundancy, reliability, and maintainability are critical issues to be addressed. To a lesser extent, the control surface authority available to maneuver the aircraft with the simultaneous implementation of active flutter suppression is also a concern. To alleviate these concerns, alternatives to utilizing the aerodynamic control surfaces for active flutter suppression are being studied.

The use of secondary controllers made of adaptive material is one such concept. There are several classifications of adaptive materials, including piezoelectrics, electrostrictors, shape memory alloys, and magnetostrictors. A detailed account of the properties, benefits, and drawbacks of each type can be found in reference 6. The present study focused exclusively on the use of piezoelectric materials, which were chosen based on their wide control bandwidth, material properties, and availability of results from previous tests. Piezoelectricity is the ability of a material to develop an electrical charge when subjected to a mechanical strain. The converse piezoelectric effect, the development of mechanical strain when subjected to an electrical field, can be utilized to actuate a structure. A local strain is produced in the structure, which induces forces and moments. By judicious arrangement of piezoelectric plates, the correct reaction of the structure required to inhibit flutter can be produced. Many research efforts have utilized adaptive plate actuators for various applications (refs. 6–17), and they have been recently used in an analytical flutter suppression study (ref. 8). Results available from aeroelastic applications of piezoceramics are very limited. Static aeroelasticity has been the subject of investigations by Ehlers and Weisshaar (refs. 6, 15, and 16). They conducted analytical studies on laminated composite wings with embedded actuators, looking at pure torsional and bending deformations. They reported that through feedback to embedded adaptive material layers, the divergence speed is altered, implying also that lift effectiveness is influenced. The augmentation or replacement of conventional aerodynamic control surfaces with strain actuation for aeroelastic control has been the focus of an analytical investigation of a typical section by Lazarus, Crawley, and Lin (ref. 17). They found that strain actuation by means of piezoelectric elements may provide a viable and effective alternative to articulated control surfaces for controlling aeroelastic response. Investigation of flutter suppression for lifting surfaces and panels has been done by Scott (ref. 8). That analytical study considered

controlling flutter at supersonic speeds by using full state feedback.

The purpose of the present study was to investigate flutter suppression by using piezoelectric plates as actuators. Results from analyses and experiments demonstrating this technology will be presented. A discussion of piezoelectric materials and some applications will be presented first. Following this, details of the experimental configuration and testing facilities are given. Development and implementation of the aeroservoelastic equations of motion are presented. Results of analytical studies based on these open loop aeroservoelastic equations, the design of the control law, and results from closed loop studies are next presented. Experimental results and comparison with analytical predictions follow. System identification test results are discussed as well as the open and closed loop flutter results.

Symbols

A	area
c	chord
d_{15}, d_{24}	electromechanical coupling coefficient, shearing response to voltage applied perpendicular to the poling axis
d_{31}, d_{32}	electromechanical coupling coefficient, in-plane response to voltage in poled direction
d_{33}	electromechanical coupling coefficient, response in the direction of applied voltage corresponding to the poling axis
E_3	applied voltage per thickness, in the 3-direction
E	Young's modulus
f	natural frequency in cycles per second (hertz)
G.F.	gauge factor
G_{12}	shear modulus
g	structural damping
I_{yy}	inertia about the pitch axis
k	stiffness of a single degree of freedom
m	mass
m_0	mass per unit area

n	number of elapsed cycles
P	transfer function
$\bar{q}$	dynamic pressure
q_{xi}, q_{yi}, q_{zi}	generalized coordinates corresponding to mode shape displacement vectors in the x-, y-, and z-directions, respectively
s	Laplace variable
T	kinetic energy
t	thickness of the piezoelectric plate
t	time
U	potential energy
u	control command in the state space equations
u, v, w	component displacements in the x-, y-, and z-directions, respectively
V	applied voltage
V_{max}	maximum voltage that may be applied to the actuator
v	velocity
x, y, z	component directions
x_n	amplitude of the nth cycle
x_0, y_0, z_0	location of the 0th point within the x, y, z frame
x_1	amplitude of the first cycle
$\bar{z}$	distance from the midplane of the plunge spring tine to the bonded face of the piezoelectric plate
γ	piezoelectric actuation constant
γ_{xy}	shear strain in the x-y plane
δ	logarithmic decrement
ε	strain
ε_{xx}	normal strain in the x-direction
ε_{yy}	normal strain in the y-direction
ζ	damping ratio
κ	curvature
λ	eigenvalue
ν	Poisson's ratio
ρ	density
σ	stress

2

σ_x	normal stress in the x-direction	**M**	generalized mass matrix
σ_y	normal stress in the y-direction	$\overline{\mathbf{M}}$	physical mass matrix (not generalized)
τ_{xy}	shear stress in the x-y plane	$\widetilde{\mathbf{M}}$	generalized mass matrix that includes the structural and aerodynamic second order terms
ω	natural frequency		

Matrices and vectors:

A	state matrix	M_Λ	moment due to strain actuation
A	extensional stiffness matrix	N_Λ	force due to strain actuation
$\widehat{\mathbf{A}}_0$	constant terms of the rational function approximation to the generalized aerodynamic forces	**Q**	generalized forces due to the aerodynamics
$\widehat{\mathbf{A}}_1$	coefficients of the first derivative terms of the rational function approximation to the generalized aerodynamic forces	$\widehat{\mathbf{Q}}$	rational function approximations to the aerodynamic generalized forces
		q	vector of generalized coordinates
$\widehat{\mathbf{A}}_2$	coefficients of the second derivative terms of the rational function approximation to the generalized aerodynamic forces	**R**	electric flux density
		S	compliance matrix
		u	control vector
B	state space control matrix	u	displacement vector with components u, v, and w
B	coupling stiffness matrix		
C	state space output matrix	**x**	state vector
D	generalized damping matrix	x_{f1}, x_{f2}	states associated with the flexible modes and their derivatives
$\overline{\mathbf{D}}$	physical damping matrix (not generalized)		
		y	output vector
$\widetilde{\mathbf{D}}$	generalized damping matrix that includes the structural and aerodynamic first order terms	β	permittivity matrix
		Γ	actuating matrix
		ε	strain vector
D	bending stiffness matrix	ϵ	impermittivity matrix
d	electromechanical coupling matrix	κ	curvature vector
		Λ	actuation strain vector
E	applied voltage per thickness	σ	stress vector
$\mathbf{F}_1$	potential energy term	Φ_{uu}	autospectrum of input
$\mathbf{F}_2$	strain actuator term	Φ_{uy}	cross-spectrum of input with output
$\mathbf{F}_3$	kinetic energy term		
G	stiffness matrix	Ψ	mode shape displacement matrix
K	generalized stiffness matrix	$\Psi_{xi}, \Psi_{yi}, \Psi_{zi}$	mode shape displacement vectors for node point i in the x-, y-, and z-directions, respectively
$\overline{\mathbf{K}}$	physical stiffness matrix (not generalized)		

Subscripts:

$\widetilde{\mathbf{K}}$	generalized stiffness matrix that includes the structural and aerodynamic zeroth order terms	a	associated with the aerodynamics
		f	associated with the flexible modes

3

i, j	ith and jth node point, mode, or element
L, M, and N	limits in the x-, y- and z-directions, respectively
p	associated with the controls or piezoelectrics
pl	associated with the plunge degree of freedom
s	associated with the structure
x, y, z	quantities in the x-, y-, and z-directions, respectively
θ	associated with the pitching degree of freedom
Λ	associated with the strain actuation
0	associated with the midplane

Operators:

$\mathcal{D}$	derivative operator matrix
dA	dummy variable of integration over the area
dV	dummy variable of integration over the volume
$\{\ \}$	vector
$[\ ]$	matrix
$[\ ]^T$	transpose
$(\dot{\ })$	derivative with respect to time

Piezoelectric Materials

A material which, when subjected to a mechanical load, accumulates an electric charge is said to have piezoelectric properties. Many naturally occurring crystals have piezoelectric capabilities, but their nonuniform properties encouraged research into manufacturing materials that would produce electromechanical coupling (ref. 18). Certain polymers and ceramics consist of crystalline subdomains that are bipolar in nature. Piezoelectric properties can be induced in these materials by applying a large electrical field across them. This induces an orientation of crystalline subdomains such that the positive and negative poles of the individual domains are aligned with the applied voltage field, denoted the 3-direction. Materials that require this poling belong to a subcategory termed ferroelectrics.

The poling process of ferroelectric materials reorients the dipoles such that there is a net polarization along the axis of applied voltage. The orientation remains after the inducing field is removed. Using these materials requires a voltage to be subsequently applied through electrodes on opposite faces of the material. The most common configuration (fig. 1) is to place the electrodes on the faces parallel to the poled axis and to apply the voltage in the same direction as the original inducing field. The material deforms both through the thickness, denoted the d_{33} effect (fig. 2), and in the in-plane directions, denoted the d_{31} or d_{32} effect (fig. 3). Applying a field oriented in one direction induces in-plane expansion; applying it in the other direction induces in-plane contraction. To define the electromechanical effects, the first subscript denotes the direction of the applied voltage and the second subscript denotes the direction of the deformation. For transversely isotropic materials, there is no distinction between vectors lying in any plane perpendicular to the poling axis. To complete the description of the deformations achievable with these materials, figure 4 shows the electrodes placed on faces parallel to the poling axis (i.e., in the 1-direction). This induces a shearing strain within the piezoelectric, as the positively poled side of the piezoceramic strains toward the negatively charged electrode and the negatively poled side strains oppositely.
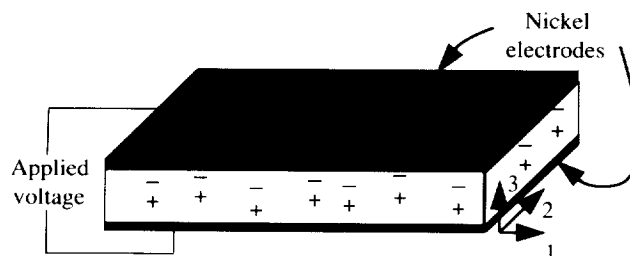

Figure 1. Electrode placement on piezoelectric plate.

Choosing the proper piezoelectric material to use for a given application is based on stiffness properties, flexibility, electromechanical coupling coefficients, and limits on applied voltage. The ability of a piezoelectric material to actuate a structure is a function of its stiffness, the limit on the voltage that can be applied across it, and the electromechanical coupling coefficients. Polymers have high voltage limits, yet they have low stiffness and low electromechanical coupling coefficients. Ceramics, on the other hand, are much stiffer and have large coupling coefficients and are thus better suited for actuator applications. Lead zirconate titanate (PZT), a piezoceramic, was
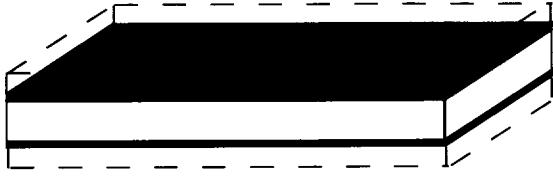
Figure 2. Thickening effect (d_{33} effect).

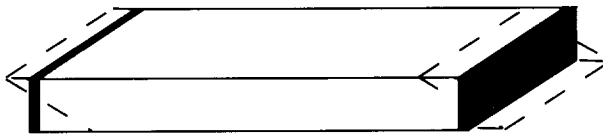Figure 3. Lengthening effect (d_{31}, d_{32} effect).

Figure 4. Shearing effect (d_{15}, d_{24} effect).

chosen for this investigation. The material properties (Product Information Catalog, PiezoSystems Solid State Motion Technologies) of the most concern in this study are listed in table I.

Table I. Material Properties for Lead
Zirconate Titanate (PZT)

Property	Value
d_{31}	166×10^{-12} m/V
d_{33}	-360×10^{-12} m/V
Maximum voltage	0.7×10^6 V/m
Young's modulus	63×10^9 N/m^2
Poisson's ratio	0.33
Density	7.65×10^3 kg/m^3

Piezoelectric plates can be configured in different ways to accentuate the displacements or forces being generated. The in-plane expansion and contraction of adaptive materials may be utilized by bonding actuating plates to either side of a center shim (fig. 5). One plate is expanded and one is contracted; the net result is a bending displacement much greater than the length deformation of either of the two layers. This configuration, which takes advantage of the Poisson-like d_{31} effect, is referred to as a bimorph
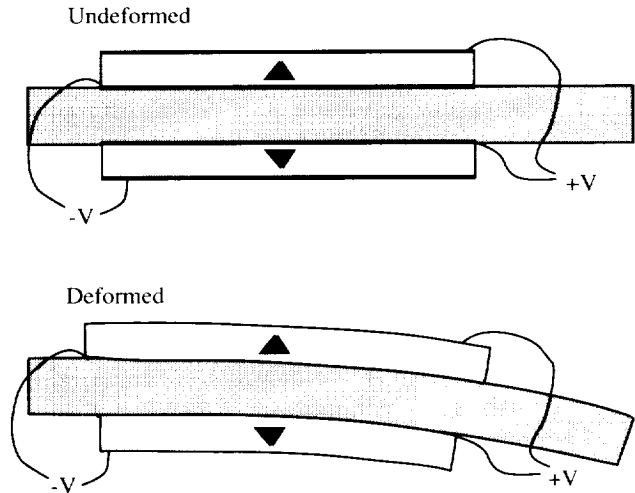
Undeformed

Deformed

Figure 5. Bimorph bender configuration of piezoelectric plate elements. For the voltage polarity shown, the top layer expands in the in-plane direction and the bottom layer contracts in the in-plane direction.

bender element. It will serve as the primary actuator mechanism for the investigation described herein.

The material properties of the piezoelectric materials have been treated in this work with linear relationships. This assumption is valid for low applied voltages and small deformations. Nonlinearities and nonidealities of these materials have been well-documented in references 6, 7, and 9. Several nonideal properties that have been found to have significance are the amplitude dependence of the field-strain relationship, creep, variations with mechanical strain, and depoling. These issues will not be addressed in detail here; however, efforts have been exerted during this investigation to avoid these nonlinear regions. The amplitude of the control signal voltage was low, thus depoling was avoided and the linear field-strain relation was maintained. The frequency of concern was approximately 10 Hz, thus creep, a low-frequency phenomenon, was avoided. The plates were also placed on a region where the mechanical strain at rest was very small, avoiding nonlinearities associated with applied mechanical strain.

Piezoelectric materials can be used in sensing and actuating applications. Piezoelectric devices used as sensors emit voltages when subjected to a mechanical load. Because this study utilized the piezoelectric plates only as actuators, sensor applications will not be discussed further. In an actuating application, the converse piezoelectric effect is utilized as the actuators deform in response to a control signal or applied voltage. The mention of actuators suggests the use of hydraulics, pistons, motors, etc. An actuator,

however, is a device that moves or causes action of something else. The use of adaptive materials in this manner has lassoed engineering interest from various areas. The following section provides an overview of several investigations that have been conducted.

In the area of rotorcraft, two distinctly different actuator configurations have been examined for higher harmonic control (refs. 9 and 10). The first used directionally attached plates to torsionally activate blade sections and actuate a trailing edge flap. The magnitude of flapping vibrations was significantly reduced with active controls. The second utilized a push-pull configuration of bender elements. Another actuating application, also detailed in reference 10, is the active damping of truss members for large space structure applications. This study used commercially available actuators that utilize the d_{33} effect (the expansion direction coincides with the direction of polarization) to limit the vibration amplitude and settling time of transients induced by dynamic perturbations to the structure, such as crew motion. In the acoustics field, recent work (ref. 12) has focused on reducing cabin noise through destructive interference produced by distributed piezoelectric plates. Separate finite impulse response filters were constructed to control an acoustic resonance and a structural mode occurring 25 percent above the acoustic resonance. Reference 13 describes the use of piezoelectric plates in a bimorph configuration on an aluminum beam in conjunction with an adaptive controller to attenuate vibrations with frequencies above 300 Hz. Reference 14 details experiments and analyses of a composite beam with distributed embedded actuators controlling structural modes from 11 to 150 Hz. Through feedback of velocity, structural damping was increased by an order of magnitude.

Experimental Apparatus

The hardware involved in this wind tunnel test is described in four sections: the wind tunnel, the test article, the digital controller, and additional instrumentation.

Wind Tunnel

The piezoelectric flutter suppression model was tested in the Flutter Research and Experiment Device (FRED) at Langley Research Center, shown in figure 6. The FRED is an open circuit tabletop wind tunnel with a maximum operating velocity of 85 mi/hr (approximately 1500 in/sec). The test section is 6 in. by 6 in. and is constructed of acrylic glass for model viewing. The air is pulled through

the tunnel by a 2-hp motor and smoothed by a single honeycomb screen at the beginning of the contraction duct. Models are mounted from the removable ceiling of the test section. Figure 7 shows the test article suspended from the test section ceiling.
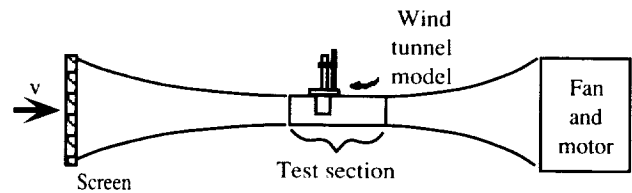

Test section: 6 in. by 6 in.
Models suspended from ceiling
Limits: Velocity–1500 in/sec (85 mi/hr)
Dynamic pressure–0.13 lb/in^2

Figure 6. Schematic of Flutter Research and Experiment Device (FRED) wind tunnel.

Test Article

The piezoelectric flutter suppression wind tunnel model (fig. 7) consists of four integral components: a flexible mount system, a rigid wing, piezoelectric plate actuators, and a strain gauge bridge. The test article was designed through an iterative procedure involving parametric studies, the details of which are presented in appendix A. There were three driving factors in the design: the model had to flutter within the wind tunnel envelope, had to fit inside the wind tunnel with certain margins of safety, and had to have flat surfaces on which piezoelectric actuating plates could be mounted. It was decided a priori that a flexible mount system would reside outside the wind tunnel and provide the degrees of freedom for a rigid wing. The physical system has two distinct structural modes. When no mass coupling is present, the lower frequency mode is a plunge mode (out-of-plane translation of the wing). The higher frequency mode is a rotation about the wing pitch axis. The wing was designed such that the modes would be coupled by virtue of the wing mass distribution.

The mount system, shown in figures 8 and 9, suspended the wing by two pins through slots in the test section ceiling and provided the plunging and pitching freedoms by virtue of separate spring tine mechanisms. The plunge mechanism consists of two spring steel plates or tines separated by 0.75 in. and clamped at both ends to maintain this distance. This provides the pure plunging motion of a beam with guided boundary conditions instead of the flapping motion associated with a cantilevered beam. The pitch mechanism is a single spring tine connected to
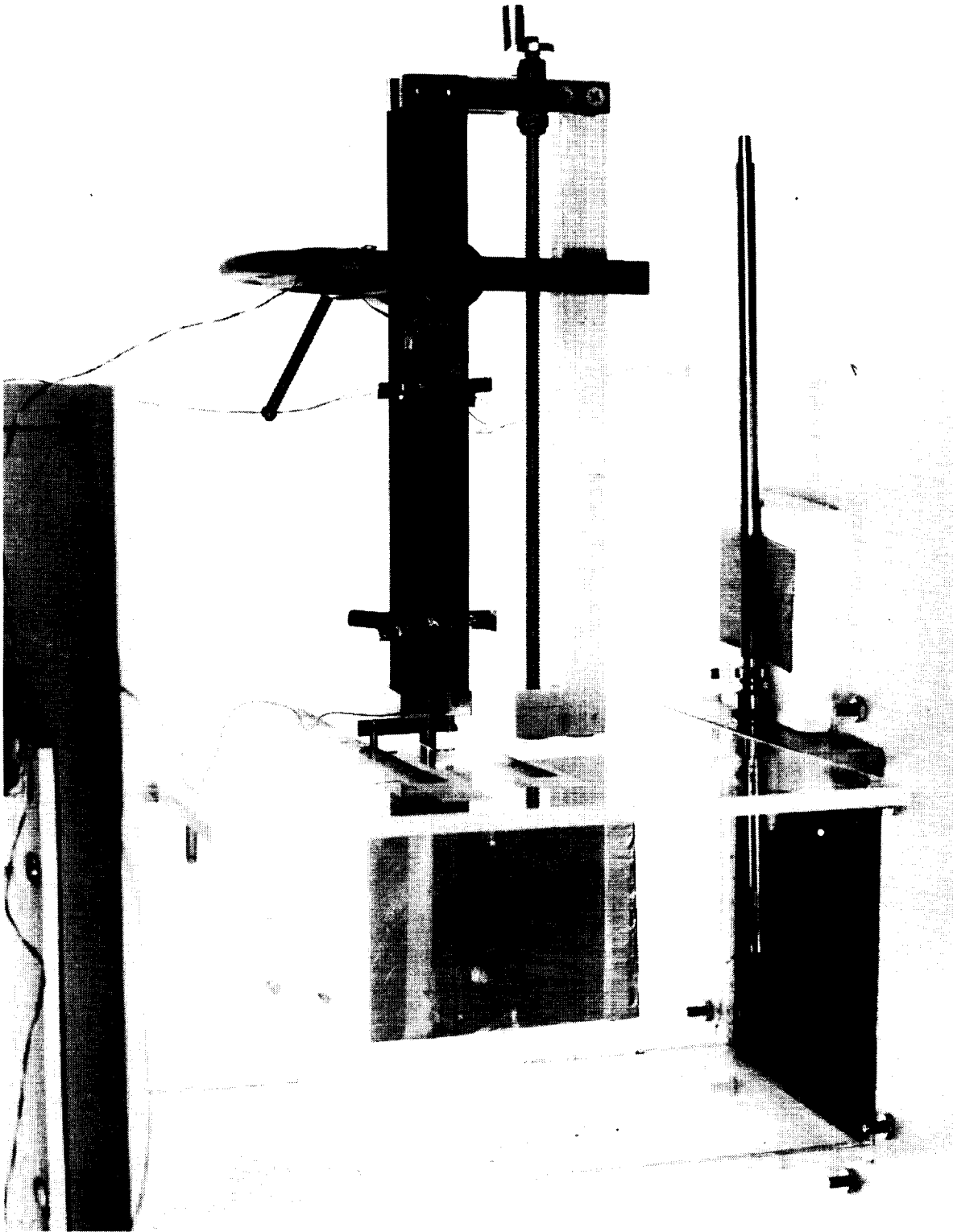
L-91-10990

Figure 7. Photograph of wind tunnel test section with test article suspended from ceiling.
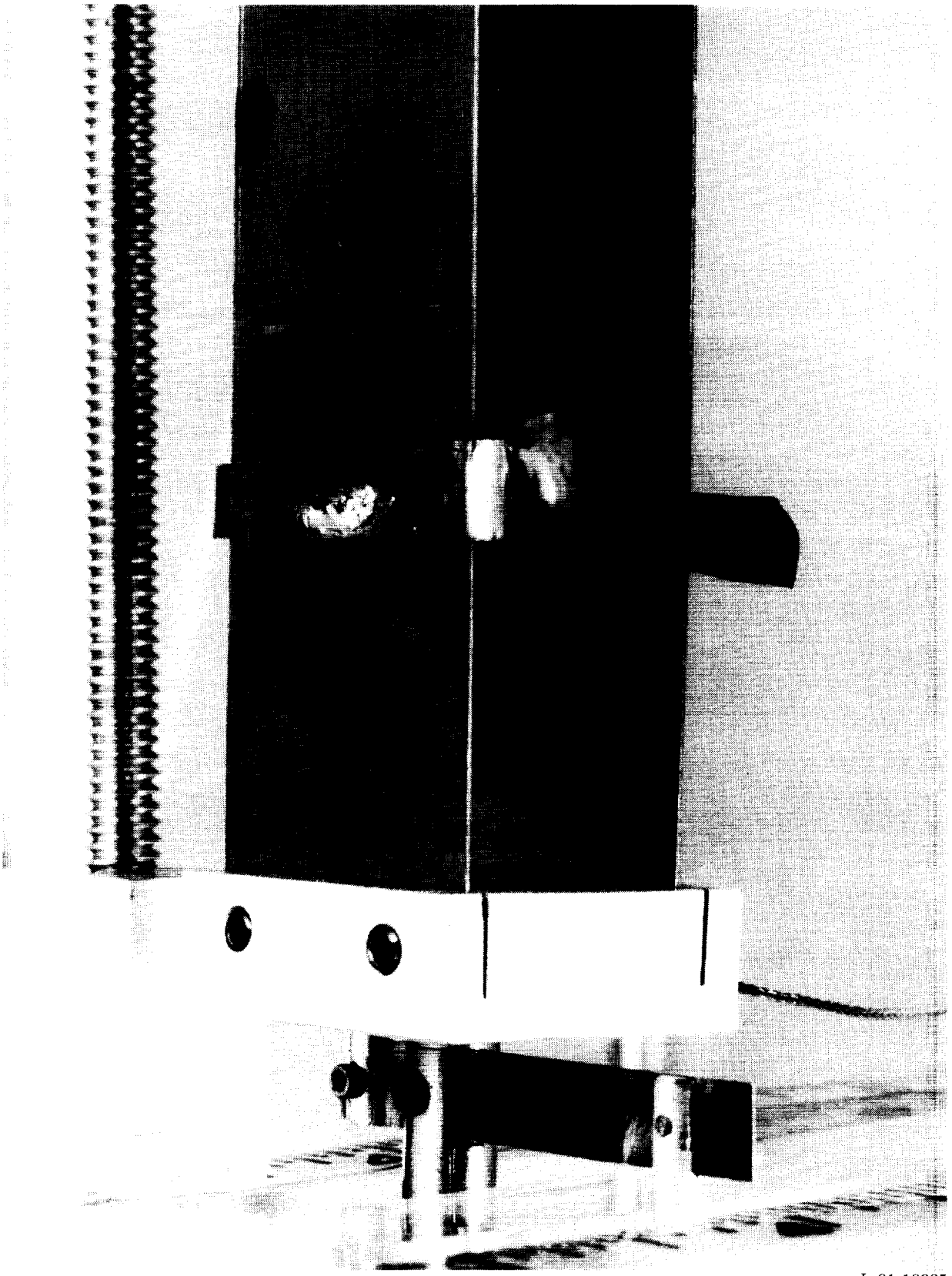
7

L-91-10985

Figure 8. Photograph of the mount system clamping block.

the wing at the leading edge and at the 0.2353-chord location, where there is a bearing-like mechanism that allows for free rotation. This configuration provides the wing with pitch stiffness and a pitch axis. The two mechanisms are joined together as shown in figure 10. The forward end of the pitch mechanism is fixed relative to the plunge springs by mounting the pitch pivot pin to the lower clamping block of the plunge mechanism.
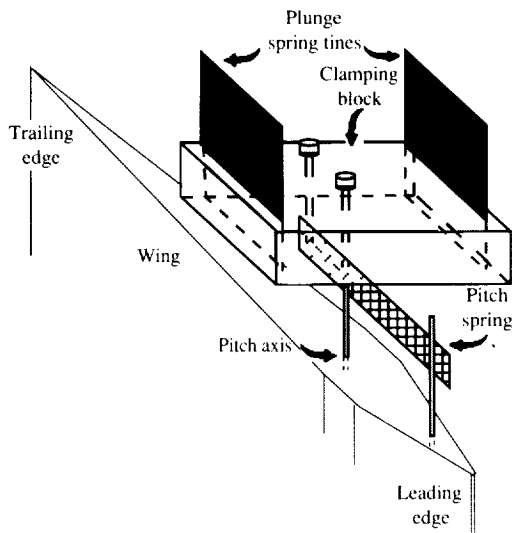

Figure 9. Mount system close-up: interconnection mechanism for the plunge and pitch degrees of freedom.
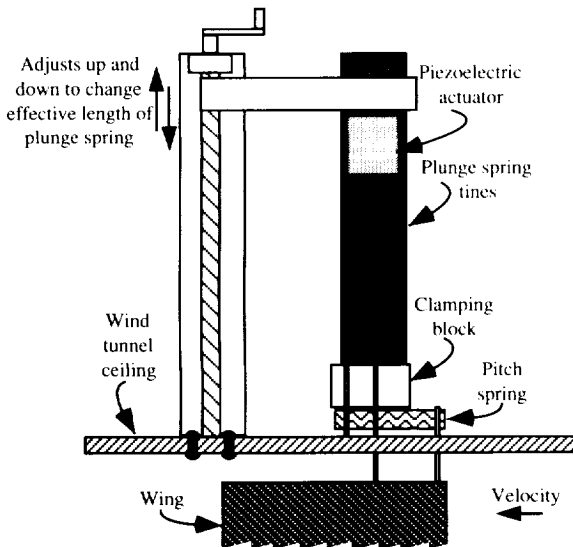

Figure 10. Wind tunnel mount system (not to scale).

The wing, depicted in figures 11 and 12, consists of three sections: an aluminum primary structure, a

balsa wood extension, and an aluminum mass ballast. The primary wing structure is formed from ⅛-in-thick isotropic aluminum with a diamond cross section and blunted leading and trailing edges and midchord section. It has a chord of 2 in., with the pitch pivot at the midchord. The balsa wood extension overlays the aft half of the primary structure and extends the chord length to 4.25 in. The trailing edge of this section was coated with aluminum to provide a mass ballast. The mass of the entire wing is 0.090 lbm and has an inertia about the pitch axis of 0.134 lbm-in². All three sections extend the full span of the wing, which is 4 in. Table II gives the measured mass and location of the center of gravity for each portion of the wing. Based on measured dimensions, mass, and distance to the pitch point, inertias for the component parts were calculated; the results are given in table III, where

$$I_{cg} = \frac{1}{12} \, (\text{Mass}) \, (\text{Width})^2 \qquad (1)$$

$$I_{pivot} = (\text{Mass}) \, (\text{Distance})^2 + I_{cg} \qquad (2)$$

Table II. Measured Mass and Center-of-Gravity Locations for Wing Components

	Mass, lbm	Center-of-gravity distance aft of pivot point, in.
Primary wing structure (includes pivot mechanism)	0.072	0.0
Balsa extension (includes adhesives)	.011	1.875
Aluminum mass ballast	.007	3.0
Total	0.090	

Table III. Inertia Calculations for Wing Components

	Mass, lbm	Width, in.	Distance, in.	I_{cg}, lbm-in²	I_{pivot}, lbm-in²
Primary wing	0.072	2.0	0.0	0.022	0.022
Wing extension	.011	3.25	1.875	.0097	.0487
Mass ballast	.007	.5	3.0	.00014	.06314

9
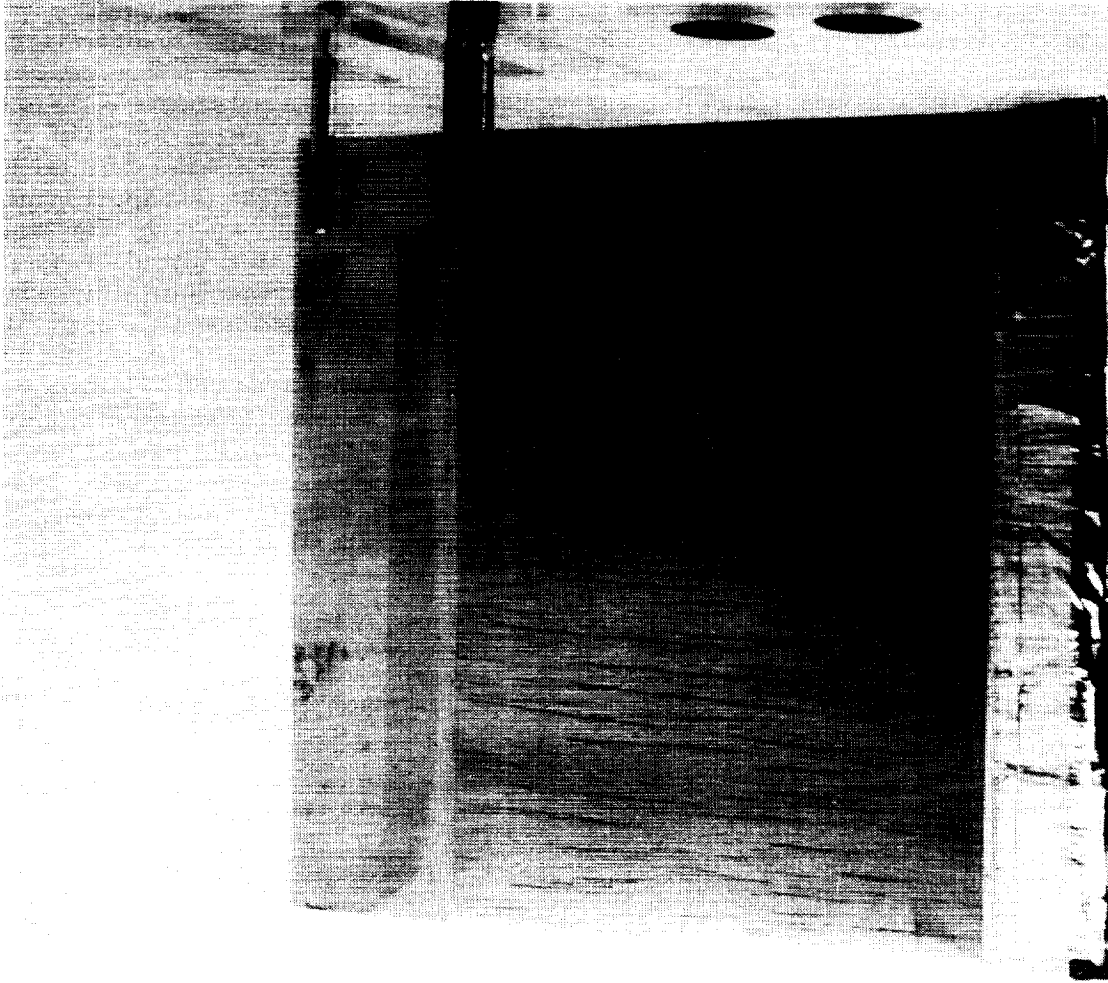
L-91-10982

Figure 11. Photograph of wing.

(a) Cross-sectional view.

(b) Planform view.
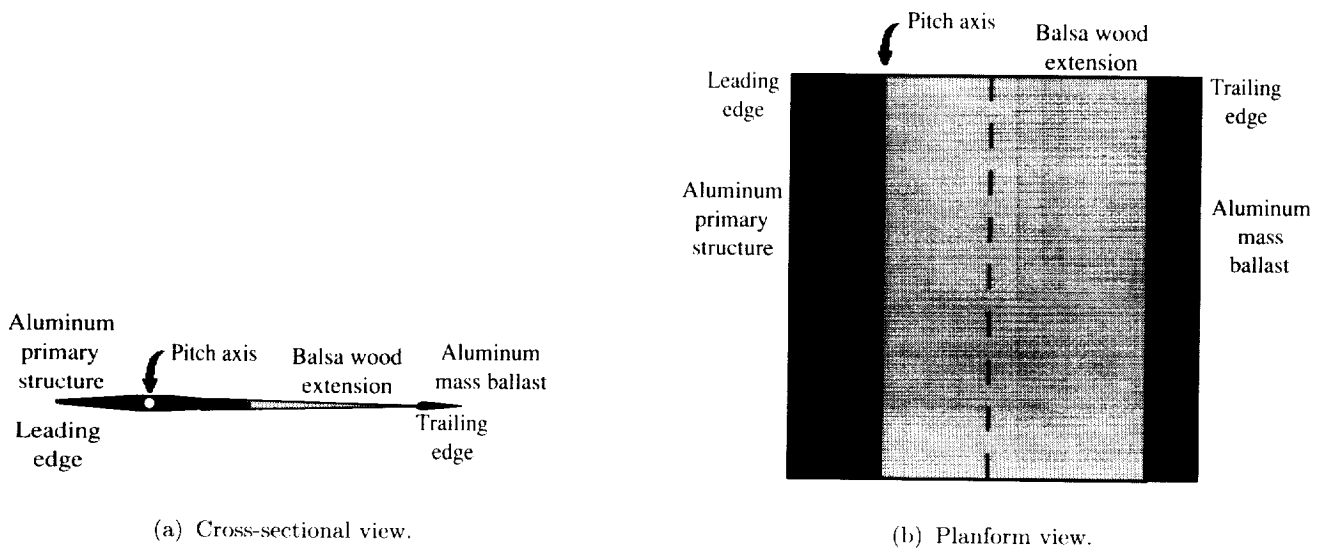
Figure 12. Schematic of wing.

10

Piezoelectric ceramic plates were installed near the root of one of the plunge spring tines to actuate the test article. Two plates, 1.5 in. long and 1 in. wide, were bonded to opposing sides of the plunge spring tine, with their positive poles both oriented toward the steel, to form a bimorph-type actuator. The 0.0075-in-thick plates were electrically isolated from the steel by the bonding layers. Small copper tabs affixed beneath the plates during the bonding process served as the means of applying voltages to the bonded-side electrodes (fig. 13).
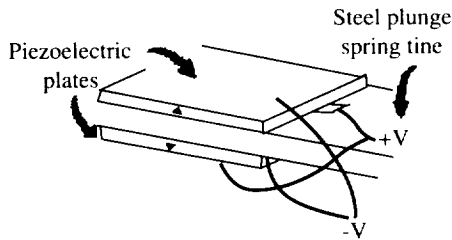

Figure 13. Piezoelectric actuator attachment to plunge spring tine.

A strain gauge bridge was mounted near the base of one of the spring tines, with two gauges on either side of the tine. The gauges can be seen in the photograph of figure 7. The gauges, which had an overall gauge factor of 2.075, were configured to measure the cantilever bending strain. The bridge was powered by a ±5-V power supply. The strain was computed by taking the ratio of the output voltage to the input voltage and dividing by the gauge factor.

$$\varepsilon = \frac{V_{out}}{V_{in}\,G.F.} \tag{3}$$

The output voltage from the strain gauge was amplified by 100 before being sent to the digital computer.

Digital Controller

The control law is implemented by using a personal computer, with an 80386 processor and an 80387 coprocessor running a real-time Unix operating system. The control laws are programmed in the C-language and use floating point arithmetic for all control law calculations. The data acquisition system uses 12-bit analog-to-digital converters (ref. 19).

Additional Instrumentation

The wind tunnel and model had three sensor systems: a strain gauge bridge, a linear accelerometer, and a hot wire anemometer. The strain gauge bridge utilized to generate the feedback measurement signal has been discussed previously.

An Endevco piezoelectric accelerometer was used in system identification experiments. It was powered by an external 4-mA current source. The output was calibrated at 9.98 mV/g. The accelerometer served as a roving sensor, being placed where applicable for different experiments. During zero-airspeed testing, it was located on the wing; however, during flutter testing, it was installed on the clamping block.

Both the strain and the acceleration were amplified by 100 before being sent to the analog-to-digital converters. The output voltage of the controller was sent to an operational amplifier having a gain of 25 and a limit on the output voltage of 80 V. This limited the usable range of output values from the controller to ±3.2 V. The amplified voltage was then applied across each of the piezoelectric elements. An Apex Microtechnology P83A operational amplifier was used to boost the input voltage to the piezoelectric actuators. The signal source or input voltage applied to the piezoelectric plates was amplified by a factor of 25, with a limit on the output voltage equal to the power supply voltage, which in this experiment was ±80 V. A block diagram of the closed loop system with active feedback is presented in figure 14. Only the signals employed in the feedback scheme are shown.

A Kurz 443M air velocity meter provided visual readouts of the test section airspeed. This is a hot film anemometer with an analog display in meters per second. The probe was inserted into the flow just behind the model in the test section. Thus, in order to accurately measure the velocity, the model must be moved to the stops to eliminate blockage and the influence of wing oscillations on the reading.

Analytical Modeling

The analytical model was developed incorporating the aeroservoelastic equations of motion, a model of the control computer dynamics, and experimentally determined correction factors. The following discussion of the analytical modeling first addresses the theoretical development of the equations of motion for an electromechanically actuated aeroelastic structure. Following this, the procedures used in generating and assembling each of the pieces of the open loop plant are presented. Details of computer software utilized for implementing the analytical model are discussed. Modeling of the control computer dynamics follows, while the final section details scaling the model for units and amplifiers along
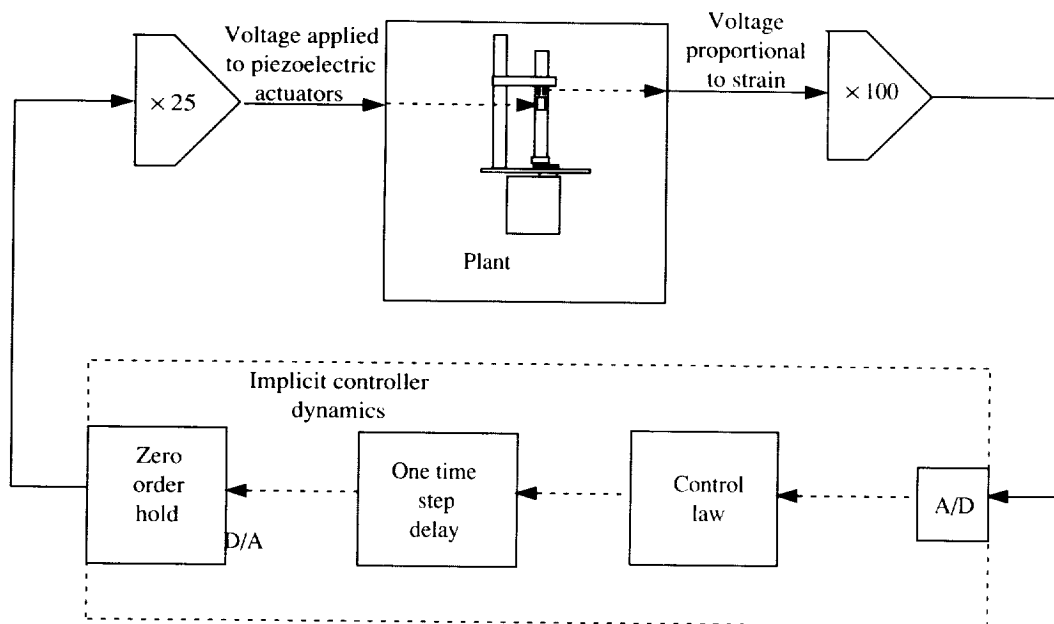
11

Figure 14. Block diagram of closed loop system with active feedback.

with incorporating the experimentally determined correction factors.

Theoretical Development of the Aeroservoelastic Equations of Motion

The aeroelastic equations of motion were developed with classical techniques available to the aeroelastic community; the control forces from the piezoelectric elements were developed with laminated plate theory in conjunction with Lagrange's energy method.

Aeroservoelastic equations of motion based on Lagrange's energy equations represent a summation of forces that include the inertial, dissipation, and internal restoring forces, the reduced-frequency dependent aerodynamic forces due to the structural motions, and the control forces. Generalized coordinates were defined as the modal contributions to the displacements. An in-depth development of the general aeroservoelastic equations of motion is presented in appendix B. To highlight the difference between an electromechanically actuated system and an aerodynamically actuated system, a brief discussion of the development follows.

Solution of Lagrange's equations requires expressions for kinetic and potential energy. The kinetic energy is defined by a volume integral, which when integrated over a uniform thickness laminate becomes an area integral, premultiplied and postmultiplied by the derivative of the generalized coordinates. The

area integral is the structural mass matrix. The potential energy is defined by a volume integral of the strain and stress vectors multiplied. The constitutive relationship that defines the dependence of strain on stress for piezoelectric materials is derived in appendix C. The modeling of piezoelectric systems requires consideration of both mechanical and electrical behavior. Coupling between mechanical stresses and electrical fields is analytically represented by constitutive relationships that contain both the electrical quantities and the mechanical quantities. This relationship is utilized in expressing the potential energy; a portion of the potential energy expression is the structural stiffness. The presence of the strain due to electrical energy generates a term that is not traditionally observed in the mechanical potential energy expression. This is the piezoelectric actuation matrix, the development of which is presented in appendix D. The calculation of this matrix is easily performed utilizing the discretized structural model. Derivatives of the expressions for kinetic and potential energy are taken as appropriate and implemented in the Lagrange equations of motion. The state vector is defined as the generalized coordinate vector and its derivative; the second order equations are thus transformed into first order state space form.

Aeroservoelastic Model Construction

A variety of techniques and software packages were employed to develop the various elements of

the equations of motion. The structural charac-
teristics were calculated by utilizing a finite ele-
ment method and normal modes analysis for de-
termining the natural frequencies and mode shapes.
Generalized aerodynamic forces were calculated from
doublet-lattice lifting surface theory applied to the
discretized wing. To implement the aerodynamic
forces in state space equations, rational function ap-
proximations were made to the tabular output of the
doublet-lattice code. The control distribution ma-
trix $\mathbf{B}$ and the output or measurement matrix $\mathbf{C}$ were
computed with finite difference techniques.

Finite element model. A finite element model
of the wind tunnel wing and the two-degree-of-
freedom mount system (fig. 15) was constructed and
analyzed with MSC NASTRAN (ref. 20). The model
developed represented the primary wing with solid
elements; the wing extension and mass ballast were
represented with concentrated mass elements. The
spring tines were modeled with plate elements. A
torsional spring was added at the pivot point to bet-
ter represent the experimentally determined pitch
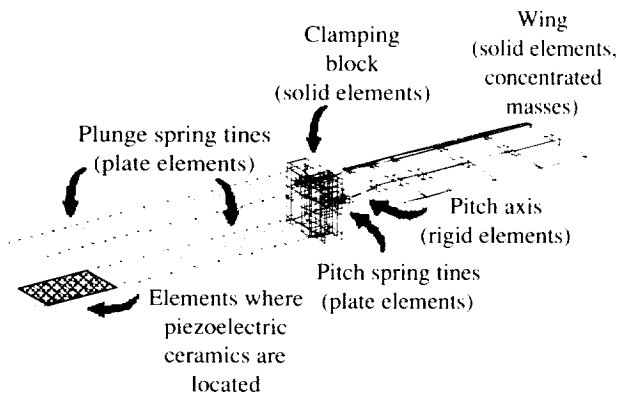frequency.

Figure 15. Finite element model.

Observation of the physical system in motion in-
dicated that the boundary condition for the plunge
spring tines was clamped or guided. The finite el-
ement model closely predicted the plunge frequency
when this boundary condition was enforced. Further
observation of the motion indicated that the pitch
spring boundary condition at the pitch pivot point
was stiffer than a cantilever, while the other end of
the tine looked cantilevered (ref. 21). The exagger-
ated sketch of figure 16 depicts this phenomenon.
From experimental frequencies and calculated iner-
tias, spring stiffness constants were computed for
three wing configurations: the primary wing struc-
ture alone, one with the balsa wood wing extension,

and one also containing a 0.007-lbm mass ballast.
From the average stiffness value, the cantilevered
stiffness of the existing finite element model was
subtracted. The resulting stiffness was included in
the finite element model by means of an explicitly
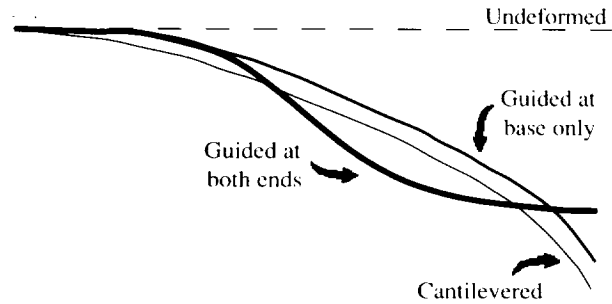modeled spring at the pitch pivot point.

Figure 16. Sketch of boundary condition influences on
deformation.

The locations on the spring tines where piezo-
electric plates were bonded were defined as compos-
ite plates, where the layers of piezoelectric ceramic
were modeled as temperature-dependent materials.
The parallel constitutive relations of thermomechan-
ical and electromechanical systems allowed the volt-
age applied to the ceramics to be represented by an
applied temperature field.

Aerodynamic model. Unsteady aerodynam-
ics were calculated with the doublet-lattice method
(ref. 22) as implemented in the Aeroelastic Vehi-
cle Analysis (AVA) system of computer codes. The
doublet-lattice method is a panel method for solving
the integral equation relating the normal wash and
the aerodynamic loading for lifting surfaces in sub-
sonic flow. Discrete lifting elements, consisting of an
oscillatory doublet line and a horseshoe vortex, ap-
proximate the loading. The steady-flow effects are
represented by the vortex; the doublet represents the
incremental effects of oscillatory, unsteady motion.
AVA uses the modal displacement vectors to cal-
culate the generalized aerodynamic forces (GAF's)
at discrete reduced frequencies. The program out-
put is a table for each reduced frequency, where the
columns of the table correspond to modal and con-
trol deflections, while the rows correspond to modal
pressures or forces. Because the wing is rigid over the
airspeed range of interest, the modal displacements
are input at six points along the leading and trailing
edges of the primary wing section. The aerodynamic
model, shown in figure 17, has 5 chordwise boxes and
10 spanwise boxes for a total of 50. The GAF's were
calculated at Mach 0.05 for eight values of reduced
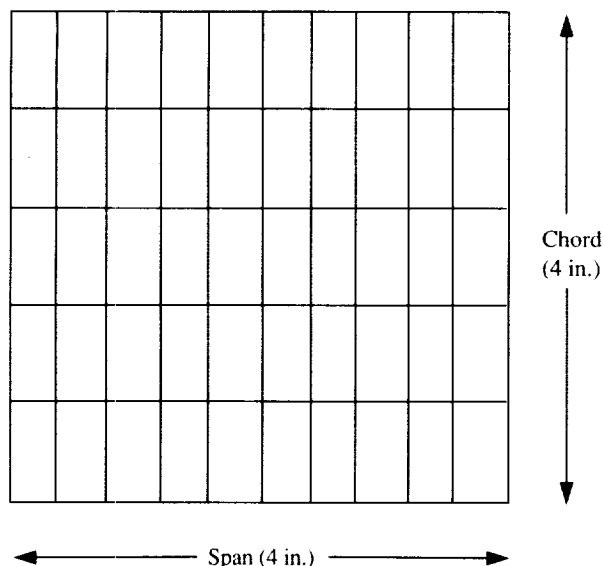frequency ranging from 0.001 to 2.0.

13

Figure 17. Doublet-lattice aerodynamic box layout.

Chord
(4 in.)

Span (4 in.)

Rational function approximations for the aerodynamics. The aerodynamics produced by the doublet-lattice code are transcendental functions of reduced frequency. In order to incorporate them into the state space equations of motion, they must be approximated by rational functions of the Laplace variable s (ref. 23). Equation (B59) illustrates the second order approximations made. The Integration of Structures, Aerodynamics, and Controls (ISAC) system of codes (ref. 24) was used to perform these approximations and generate the resultant s-plane GAF's. The objective of the fit is to determine the coefficients such that the approximation best fits the tabular data in a least-squares sense subject to a set of linear equality constraints imposed upon the coefficients. The constraints imposed for this model are that the approximations will exactly match the tabular values at zero reduced frequency for each of the modes. Figure 18 shows the GAF's plotted as a function of reduced frequency and the results of the approximation.

Finite difference program for generating the actuating matrix. The actuating matrix Γ is calculated by a finite difference program. This code calculates the second derivative at the center of each of the structural elements by using the displacements two node points from both sides of the element. The only elements included in this calculation are those laminated with the piezoelectric plates. The actuating plates near the root of a plunge spring consist of six elements, each 0.25 in. long and 1 in. wide. The displacements are assumed to be constant

across the width of the spring tine, so only one row of displacements along the length is used in the calculations.

Finite difference program for modeling the strain gauge. Strain gauges configured to measure cantilever bending are also governed by the behavior of the second derivative of the motion, taken with respect to the lengthwise coordinate (ref. 25). The same basic program used in calculating the actuator influence matrix was modified to calculate the strain gauge coefficients. The second derivative was calculated at locations near the root of the plunge spring and multiplied by the spring tine thickness to predict the strain on the surface.

Generating the state space equations of motion. The equations of motion were assembled with MATRIX$_X$, a commercially available software package from Integrated Systems, Inc. (ref. 26). The continuous, open loop model was generated in first order form. The procedure, given in table IV, shows the details of the A and B matrix calculations and the C matrix for strain gauge measurements. These matrices are then discretized with the appropriate sample rate.

Modeling the Control Computer Dynamics

The influences of the zero order hold and one time step delay on the closed loop system were examined using Matlab, a commercially available software package from MathWorks, Inc. (ref. 27). The influence of the sample rate was also determined. MATRIX$_X$ implicitly models both the zero order hold and a one-sample delay automatically when the discretization command is used.

Illustrated in figure 19 for a gain feedback control law, the control computer introduces its own dynamics into the feedback path. The digital controller implementation scheme shifts the output data by one sample and applies a zero order hold. The frequency response of the digital controller is different for different sample rates. Using a sample rate that emulates analog derivative feedback near the frequency of control interest allows the system to simulate derivative feedback, despite having only displacement measurements (ref. 28). The current control law utilizes the dynamics of the implementation scheme, requiring only gain feedback. The frequencies of concern lie between 7.9 and 11.1 Hz. Figure 19 shows that for a 20-Hz sample rate, the phase is $-270°$, or $+90°$ at 10 Hz. Thus, the phase characteristics simulate a derivative in the frequency range of interest, near 10 Hz.
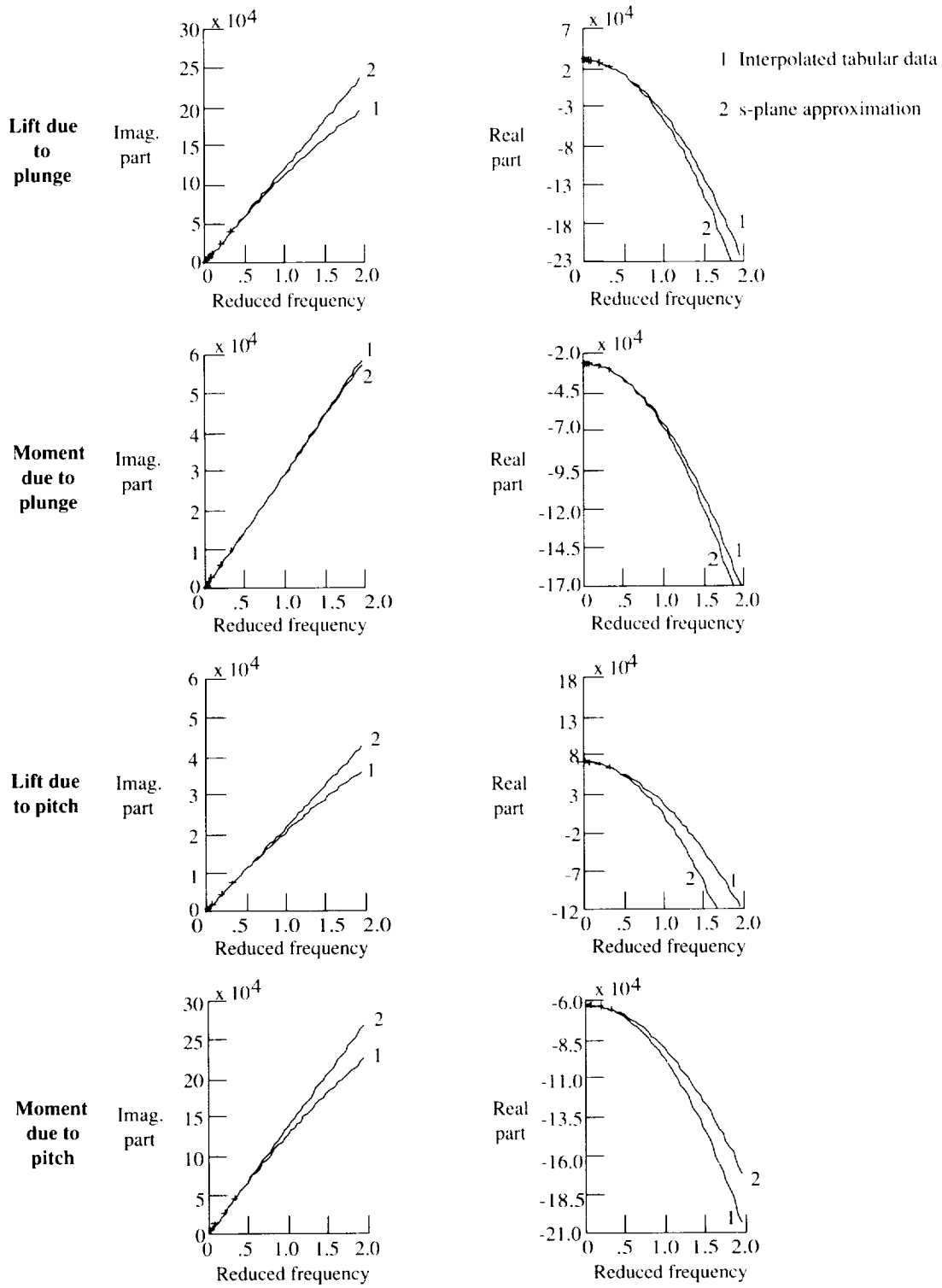
Figure 18. Rational function approximations to the generalized aerodynamic forces.

Table IV. MATRIX$_X$ Command File for Assembling the Equations of Motion

```
//
//eom.mat
//
// Procedure file used to generate open
loop equations of motion
//
// Gamma is the finite difference program
output matrix which
//   calculates the piezoelectric
structural influence
//
// Cstrain is the second derivative of
each of the mode shapes
//   with respect to lengthwise coordinate
//
// Physical parameters
chord=4.0
rho=.11468e-6
d31=-6.35e-9
qbar=.5*rho*v**2
//
// Structural stiffness, damping, and mass
//
omega=[7.8;10.89]
freq=2*pi*omega
dsi=[.017 .055]
ms=[eye(2)]
ks=diag(freq.**2)*ms
ds=diag(dsi)*diag(freq)
//
// Aerodynamic stiffness, damping, and mass
//
ma=qbar*(chord/2/v)**2*a2
da=qbar*chord/2/v*a1
ka=qbar*a0
//
// Combining aerodynamic and structural
matrices
//
m=ms+ma
minv=inv(m)
d=ds+da
k=ks+ka
//
// Assembling the state space matrices
//
a=[0*ones(2,2)eye(2,2);  -1*minv*k-1*minv*d]
//
bs=-1*d31*minv*gamma
b=1.2*[0;0;bs]
zbar=.008
c=-1.3*zbar*cstrain
s=[a b;c 0*ones(2,1)]
```
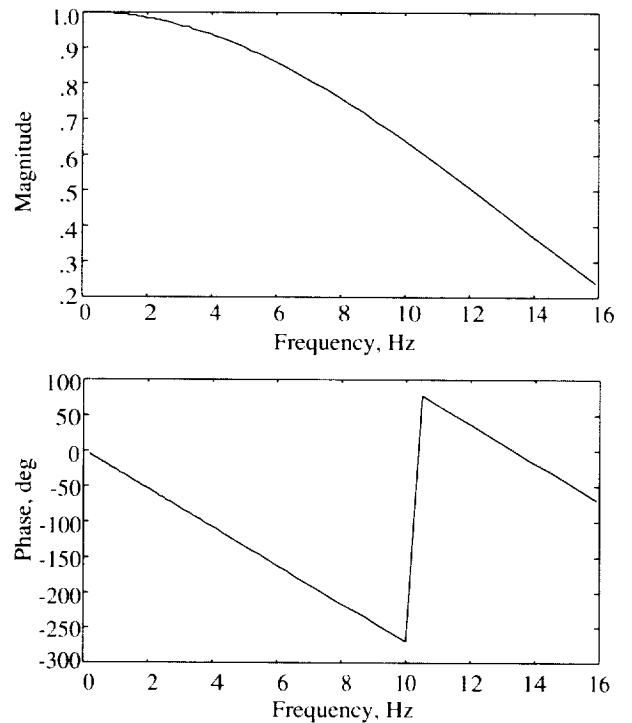

Figure 19. Frequency response of implicit controller dynamics for 20-Hz sample rate (time delay and zero order hold).

Scaling and Correction Factors

The experimental setup contains amplifiers, discretizations, etc., which must be included in the analytical model if a controller design is to be applied to the physical system. The strain produced on the model is measured by gauges that produce voltages. These voltage levels are insufficient for the digital controller to discern. Thus, an amplifier with a gain of 100 is introduced into the strain path. It must also be kept in mind that the strain is not actually fed back, but a voltage proportional to strain. Any control law generated must account for this factor. The feedforward path, from the control computer to the piezoelectrics, also contains an amplifier, which multiplies the input by 25. This gain is included in the computation of control matrix **B**.

The equations generated contain errors due to inability of theory to predict physical phenomena, shortcomings in methods used, neglected terms, and nonidealities of the physical model. The computation of the strain gauge values by a finite difference technique had an error of 30 percent at zero frequency. Because the differencing was performed on plate elements very near the clamped boundary condition, it was determined that the values yielded were

inaccurate. The strain gauge equations were scaled by 1.3 to account for this. Zero frequency gains were also computed experimentally for the transfer function from the piezoelectric voltage to the strain gauge output. They were off by 20 percent. This was anticipated because of the unmodeled bonding layer. The control matrix was multiplied by 1.2 in an attempt to correct for this difference.

Analyses

Analyses were performed with the aeroservoelastic equations of motion derived and implemented as detailed in the previous section. Results from these analyses are discussed in three sections: (1) finite element model studies, (2) aeroelastic analyses of the open loop system, and (3) control law design and closed loop analysis.

Results from system identification tests, which will be detailed in the experimental section of this paper, were incorporated into the aeroservoelastic equations of motion prior to the open loop analysis. These experimental results include natural frequencies, structural dampings, and scale factors for the actuator and the sensors.

Finite Element Analysis

The finite element model served several purposes: (1) the structural matrices were generated, (2) natural frequencies and mode shapes were calculated by performing a normal modes analysis, (3) a parametric study was performed to design the mass ballast, and (4) parameter variations were performed to determine the placement of the actuating plates necessary to obtain the maximum control effect.

After the construction of the structural mass and stiffness matrices, normal mode analysis was performed to generate natural frequencies and mode shapes:

$$\left[\overline{\mathbf{K}}_s - \lambda_i \overline{\mathbf{M}}_s \right] \{ \mathbf{\Psi}_i \} = 0 \qquad (4)$$

The natural frequencies were calculated from

$$f_i \, (\text{Hz}) = \frac{1}{2\pi} \sqrt{\lambda_i} \qquad (5)$$

The resulting undamped mode shapes $\{ \mathbf{\Psi}_i \}$ are orthogonal and, like any eigenvectors, can be arbitrarily scaled. It is a common practice in aeroelastic modeling to scale them such that a unit generalized structural mass matrix is generated:

$$\mathbf{M}_s = [\mathbf{\Psi}]^{-1} \, \overline{\mathbf{M}}_s \, [\mathbf{\Psi}] = [I] \qquad (6)$$

Predictions of the natural frequencies are presented in table V for various pitch boundary conditions with and without piezoelectric plates incorporated. The pitch spring boundary condition was enforced first as a cantilever and second as a combination of cantilevered and guided boundary conditions. The combination of boundary conditions was enforced to increase the pitch spring stiffness to the value indicated by experimental results. The finite element model was augmented with the piezoelectric actuators and reanalyzed. The presence of the piezoelectric plates increased the open loop stiffness; the plunge frequency increased by 15 percent.

Bernoulli-Euler beam theory calculations provided valuable benchmarks for the frequency results. Reasonableness checks were performed by comparing idealized beam theory for cantilevered and guided boundaries with the finite element results. The influence of the piezoelectric elements on the mass and stiffness properties is neglected in these calculations. The two degrees of freedom are considered as completely decoupled. The plunge spring was modeled with a cantilevered boundary condition, while the pitch spring stiffness was computed for cantilevered and then guided boundary conditions. The frequency predictions are presented in table V.

The most accurate system model was deemed to be the finite element representation that included the combined guided and cantilevered pitch spring model with the piezoelectric plates in place. The vibration mode shapes are shown in figure 20. The first mode, designated plunge because of the dominance of translational motion, was predicted at a frequency of 7.8 Hz. The second mode, which is characterized by the pitching of the wing relative to the mount system, has a natural frequency of 10.9 Hz.

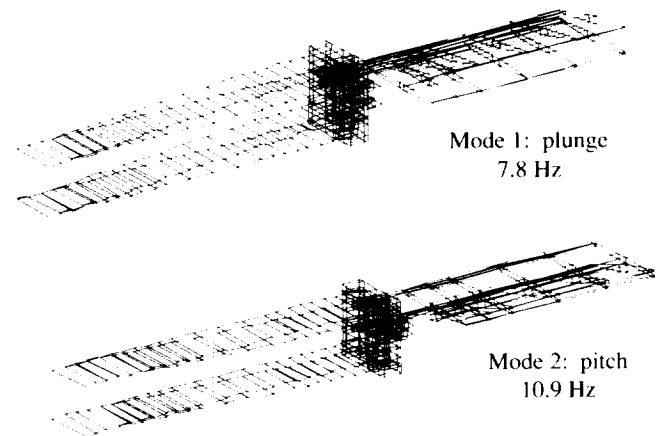Mode 1: plunge
7.8 Hz

Mode 2: pitch
10.9 Hz

Figure 20. Finite element analysis vibration mode shapes.

Table V. Analytical Predictions of Natural Frequencies
With and Without Piezoelectric Actuators

	Pitch spring boundary condition	Plunge mode frequency, Hz	Pitch mode frequency, Hz
Without piezoelectric plates:			
Beam theory	Cantilevered	7.2	6.7
Beam theory	Guided	7.2	13.4
Finite element model	Cantilevered	6.6	9.2
Finite element model	Combined	6.8	10.6
With piezoelectric plates:			
Finite element model	Combined	7.8	10.9

Prior to the analysis presented above, the mass and inertia properties of the physical configuration had to be settled. A study to determine the amount of mass ballast desired was performed with the finite element model. The natural frequencies of the system are dependent upon the mass distribution:

$$\omega_{pl} \propto \sqrt{\frac{k_{pl}}{m}} \qquad (7)$$

$$\omega_\theta \propto \sqrt{\frac{k_\theta}{I_{yy}}} \qquad (8)$$

The total mass of all components supported by the plunge spring tines, m, is used in the calculation of the plunge frequency. The inertia used in the calculation of the pitch frequency is the inertia of the entire wing about the pitch axis. The mass ballast, located at the trailing edge, contributes significantly to the inertia. The flutter speed is shown in appendix A to be sensitive to frequency separation. Thus, the flutter characteristics can be adjusted by slight modifications to the mass ballast. Table VI compares the analytical predictions of the natural frequencies for mass ballasts from 0.005 lbm to 0.011 lbm. It also shows the natural frequencies of the primary aluminum wing with no extension or ballast and of the wing with only the balsa wood wing extension.

Another study was performed to determine the optimal placement of the actuating plates. By using 1-in-long piezoelectric segments, a pair of actuators was analytically placed at different locations on the plunge spring tines. Table VII shows the displacement generated at the "free" end for different actuator locations and identical applied voltages. In

Table VI. Influence of Mass Ballast on Analytical
Predictions of Natural Frequencies

	Pitch frequency, Hz	Plunge frequency, Hz
Primary wing	25.78	8.96
With wing extension only	13.29	8.38
Mass ballast, lbm:		
0.005	11.39	7.99
.007	10.86	7.79
.009	10.65	7.61
.011	10.41	7.40

Table VII. Results of Study To Determine
Actuator Placement

Distance from root to edge of piezo, in.	Plunge mode frequency, Hz	Pitch mode frequency, Hz	Model deflection, in.
No piezo present	7.02	12.6	0
0.25	7.77	12.7	-9.21×10^{-5}
1.25	7.26	12.6	-5.69×10^{-5}
2.25	7.02	12.5	-1.54×10^{-5}
3.25	7.02	12.5	2.59×10^{-5}
4.25	7.30	12.6	6.77×10^{-5}
5.25	7.75	12.6	9.47×10^{-5}

reference 7 it was found that the actuators should be placed in regions of high strain for the mode that is of control interest. By virtue of both maximum deflection and maximum strain, this investigation indicated that the actuating plates should be placed near either end of the clamped spring tine.

Open Loop Aeroelastic Analysis

Flutter analysis of the model was conducted by analyzing the open loop aeroelastic equations of motion at a given density for various velocities (ref. 29). As the velocity changes, the relative influence of the aerodynamic and structural contributions to the inertial, damping, and stiffness characteristics of the system changes. The velocity root locus plot of figure 21 shows the open loop flutter characteristics. The plot traces the roots of the system as the airspeed is increased. The horizontal axis is the real part, while the vertical axis is the imaginary part. The imaginary axis represents the point of neutral stability or zero damping, where, theoretically, responses will neither converge nor diverge. Flutter, defined as an oscillatory divergence, is represented on a root locus plot by an eigenvalue crossing this axis into the right half plane.
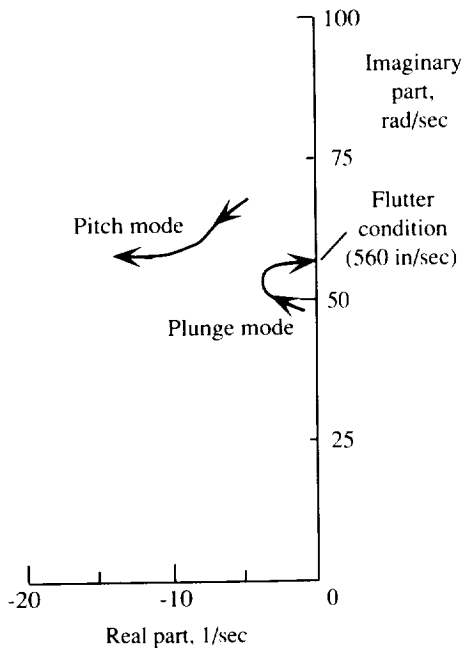

Figure 21. Root locus (eigenvalue locations as velocity is varied).

Figure 21 predicts the behavior of the plunge and pitch modes for sea level density. The frequencies of the two modes migrate toward one another as the aerodynamics couple the two modes. When the frequencies are close together, the modes interact with one another and the system is driven unstable, shown by the plunge mode eigenvalue crossing into the right half plane. The predicted flutter mechanism involves the coalescence of the plunge and pitch modes at a velocity of 560 in/sec and at a frequency of 9.1 Hz.

An alternate method of expressing the same data is to plot the frequencies and the damping ratio as functions of velocity. This method will be discussed later in the comparison of analysis and experiment.

Control Law Design and Closed Loop Analysis

The control law design requirement for the current study was to suppress flutter over a velocity range. There was no performance requirement besides stability. Because of the simplicity of both the design objective and the test article, the aeroelastic phenomenon was controllable through a single-input single-output control law. Gain feedback (ref. 30) utilizing the dynamics of the discretization process was employed. The strain-proportional voltage was the input to the control law.

Saturation places limits on the implementable feedback gain. In a traditional aircraft control scheme, the gains are restricted by aerodynamic saturation of the control surfaces as they stall or by the limits of hydraulic actuators. In this experiment, the piezoelectric actuators were capable of handling more voltage than the operational amplifier was capable of producing. Thus, the maximum voltage of the amplifier, not the limiting voltage of the piezoelectric plates, became the limiting value. The amplifier had an output limit of 80 V; input voltages were amplified by 25. Thus, the maximum input voltage was 3.2 V.

$$\text{Maximum gain} \times \text{Maximum strain response} \leq 3.2 \text{ V} \quad (9)$$

The open loop strain response had a maximum measured voltage of 0.097 V for wind tunnel conditions just below flutter. Thus, the usable gain was limited to 33.

In the implementation of the control law, the signal was discretized by a 20-Hz sampler and multiplied by the feedback gain. Digital-to-analog converters held the output data until the end of the sample period. The output signal was then updated. This value was held until the end of the next sample period, when new output data were available. References 31 and 32 provide more detailed explanations of this digital-to-analog conversion, called a zero order hold. Detailed characterization of the dynamics of the control law computer was discussed under the analytical modeling section; their influence has been included in the following analyses.

Control law design is traditionally performed in the continuous domain. Because the control law computer dynamics were an integral part of this design,
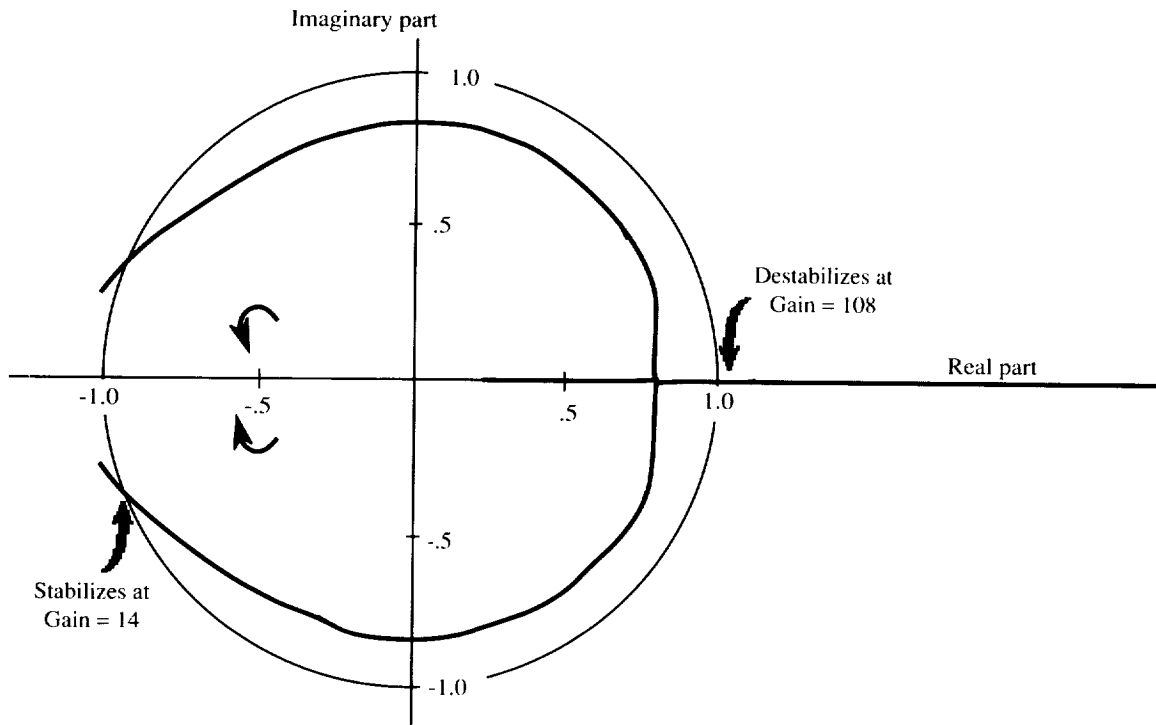
Figure 22. Gain root locus of the discrete system at open loop flutter; 580 in/sec with gains from 0 to 120.

however, the discrete domain model was utilized in this investigation. On a diagram of discrete system eigenvalues, the stability condition corresponds to the location of the roots relative to the unit circle. Roots outside the unit circle correspond to instabilities. That is, the imaginary axis of the continuous complex plane maps to the unit circle of the discrete complex plane.

Design models were constructed from the aeroservoelastic equations of motion developed in the previous section. Because these equations contain velocity-dependent terms, models were created at several distinct velocities. The equations representing the system at the predicted open loop flutter condition, determined to be 580 in/sec, were the initial design model. The continuous model was discretized with a 20-Hz sample rate. A gain root locus, constructed by varying the gain from 0 to 120, is shown in figure 22. Each eigenvalue trace begins at the open loop system values that correspond to a feedback gain of zero. One pair of roots shown in figure 22 is unstable for the open loop case, as this velocity corresponds to the open loop flutter condition. The flutter mode eigenvalues stabilize for small feedback gains, since they migrate inside the unit circle almost immediately. As the

gain increased, the eigenvalues continued to migrate within the unit circle for feedback gains up to 108, where one destabilized again.

The stability criterion can be expressed as a limit on the magnitude of the eigenvalues. The magnitude of the largest eigenvalue must be less than 1.0 for the system to be stable. Figure 23 shows the value of the maximum magnitude of the eigenvalues plotted against feedback gain. The design model, linearized at 580 in/sec, stabilized for gains higher than 14 but less than 108. As the gain increased from 0 to approximately 45, the system became more stable; additional gain did not decrease the eigenvalue magnitude. This model, however, represented the system at only one airspeed. The same figure shows the variation with gain for several airspeeds. For 1 in/sec airflow, the model was open loop stable. As the gain increased, there was very little change in the eigenvalue magnitude until the gain reached 102. The magnitude increased and the system was driven unstable for gains of 104 and above. The maximum airspeed for which gain feedback stabilized the system was found to be 1300 in/sec. As indicated in the figure, gains between 103 and 108 stabilized the system at this airspeed. If physically attainable and no stability margins are required,

20

103 is the optimal gain. Practical limitations on the gain, however, did not allow a gain of this magnitude to be implemented.
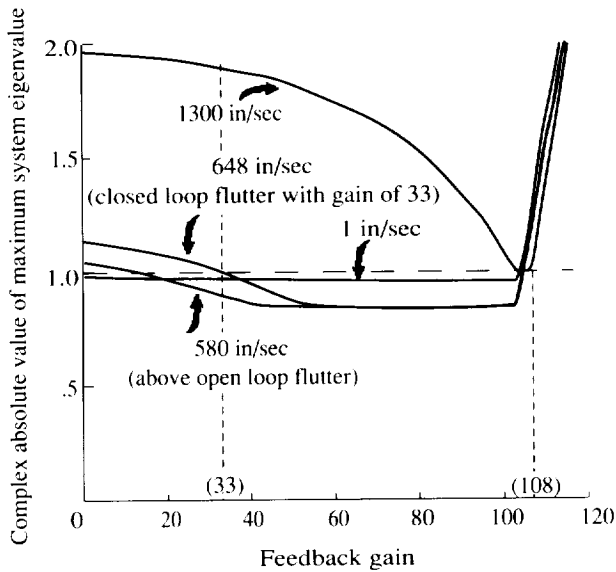

Figure 23. Maximum complex absolute value as a function of feedback gain for various airspeeds.

A velocity root locus was constructed with the largest allowable feedback gain, 33. Figure 24 shows the traces of the eigenvalues as the velocity is increased from 0 to 700. As with the gain root locus, a stable system has eigenvalues all lying within the unit circle. The flutter mode initially stabilized and then slowly began to migrate back toward the unit circle. The root crossed the stability boundary, predicting closed loop flutter at 648 in/sec. The previous graph (fig. 23) showed the variation of maximum eigenvalue magnitude as a function of gain for this velocity. The influence of increasing velocity can also be seen on this graph by examining the dashed vertical line representing a feedback gain of 33. At 1 in/sec, the eigenvalue is just below the stability point, 1.0. The next higher velocity plotted is the open loop flutter speed, 580 in/sec. The eigenvalue magnitude has decreased, indicating the stabilizing effect of the feedback. For a velocity of 648 in/sec, the trace intersects the stability boundary. Recall that this is the closed loop flutter speed. For velocities greater than the closed loop flutter speed, there is a substantially increased magnitude of instability. This is illustrated by the data corresponding to a velocity of 1300 in/sec.

Initial parametric studies, presented in appendix A, indicated that separation of the zero-airspeed
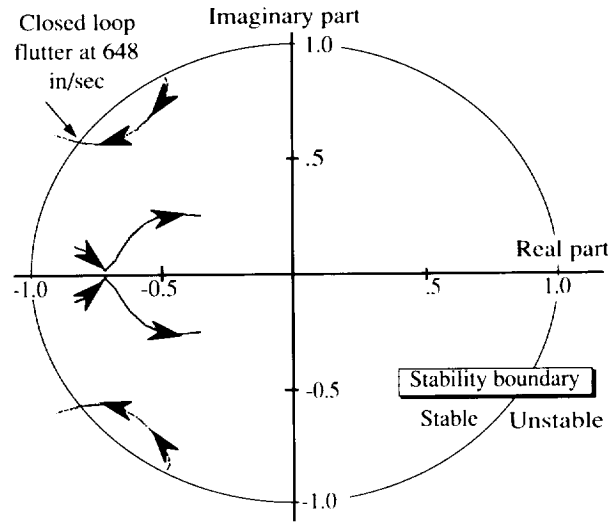

Figure 24. Discrete system root locus for varying velocity of the closed loop system with feedback gain of 33.

natural frequencies, or undamped natural frequencies, would have the effect of delaying the onset of flutter. A comparison between the open and closed loop eigenvalue magnitudes for increasing velocities is presented in figure 25. The effect of the gain feedback is shown to separate the natural frequencies as the aerodynamic influence grows (i.e., the velocity gets larger, increasing the magnitude of the aerodynamic contributions to the mass, damping, and stiffness matrices).
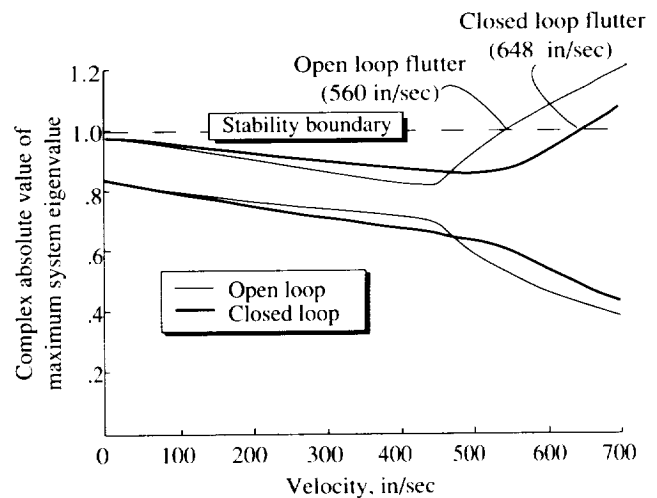

Figure 25. Open and closed loop complex absolute value of maximum system eigenvalue versus velocity with 20-Hz sample rate and feedback gain of 33.

Analytical Results Summary

The finite element results indicated that the piezoelectric plates should be placed near the ends

of the spring tines. The natural frequencies predicted were 7.8 and 10.9 Hz. The results of the open loop aeroelastic analysis indicate the onset of flutter at 560 in/sec. With gain feedback at a gain of 33, and control law computer dynamics imparted by a 20-Hz sample rate, the closed loop flutter speed is predicted to improve by 15.7 percent.

Experiments

Experimental results from bench tests and wind tunnel tests are presented in this section. Bench tests yielded scaling factors for the feedback sensor and actuator and provided zero-airspeed system identification results. The wind tunnel results to be discussed include system identification and flutter testing.

Experiments were performed at various points during this project. Static testing was performed on the model to check and determine gains within the open loop system. This was a very useful test because of the many component parts that were necessary to conduct the sensing and actuating. Open and closed loop flutter tests were conducted and the results compared with one another as well as with analytical predictions.

Static Testing

Static testing was performed on the model to determine open loop system gains. To validate and correct the mathematical model, an experiment was devised to check the strain gauge coefficients. A known displacement was applied to the clamping block (fig. 9); the strain was measured. Applying the same amount of displacement to the mathematical model yielded a strain 30 percent smaller. The sensor equations associated with the strain gauge were increased to give the correct dc value. With the strain equation yielding the experimental value, a constant voltage was applied to the piezoelectrics and a strain was measured. The mathematical model predicted 20 percent less strain than the measured value. The control matrix was then scaled to yield the correct value.

System Identification Testing

System identification testing was performed using several techniques to extract modal frequencies, dampings, transfer functions, and general system behavior. There were several experimental and analytical techniques used to extract these system parameters (fig. 26). Impulse response functions of the accelerometer generated by hammer tests proved to be the most reliable means of extracting the natural frequencies of the system, but could be used only
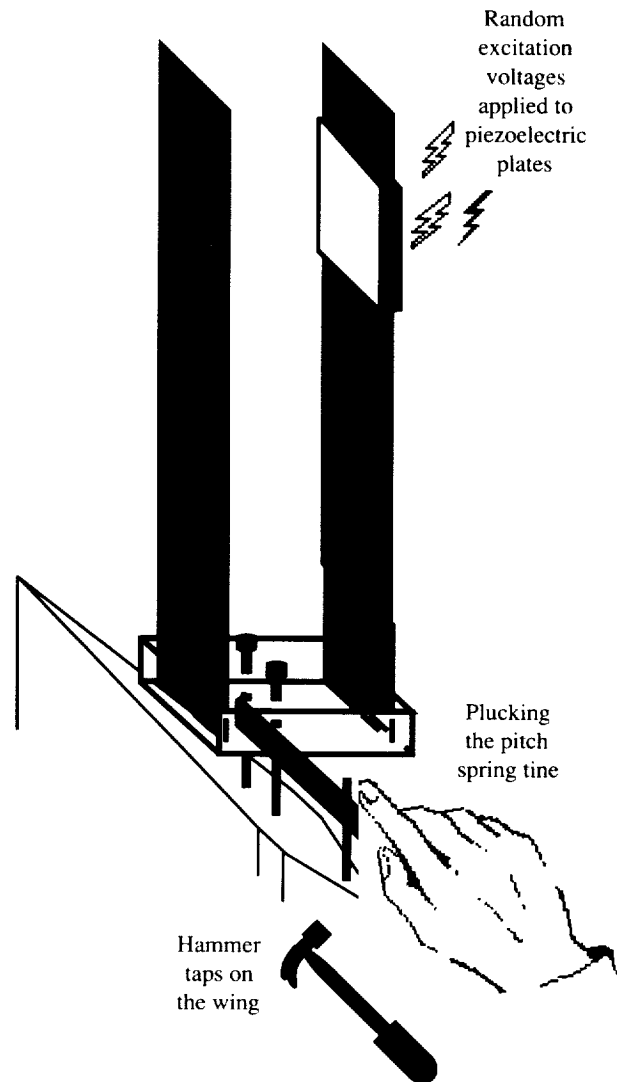

Figure 26. Experimental system identification techniques.

at zero airspeed because the wing could not be directly accessed while in the tunnel. Additionally, the amount of disturbance introduced to the flow by the presence of the accelerometer and its lead wire drastically altered the aerodynamic behavior. A second technique, employed to obtain a more dramatic response from the pitch mode, was to pluck the spring tine and record the free-decay data. This free-decay technique was effective at low airspeeds, where the plucking did not perturb the model enough to induce large oscillations. The third technique was to excite the model by applying random voltage to the piezoelectric actuators. There were several advantages to this method—most importantly, the actuator influence was included in the results. Also, because the amplitude of the input could be carefully controlled,

this technique could be used throughout the test envelope without inducing flutter. By examining the recorded input and recorded sensor output, transfer functions could be calculated.

Two of the three methods involve the calculation of transfer functions. This is accomplished by reading the time histories into Matlab and transforming them, by fast Fourier transforms (FFT), into the frequency domain. The autospectrum of the input Φ_{uu} and the cross-spectrum of the output with the input Φ_{uy} are calculated:

$$\Phi_{uu} = \text{FFT}\,(u) \times \text{FFT}\,(u) \qquad (10)$$

$$\Phi_{uy} = \text{FFT}\,(u) \times \text{FFT}\,(y) \qquad (11)$$

The transfer function is the ratio of the cross-spectrum over the autospectrum:

$$P\,(s) = \frac{\Phi_{uy}}{\Phi_{uu}} \qquad (12)$$

Details of the specific tests are now presented.

Impulse tests. Hammer taps to produce impulse inputs were used at zero airspeed to extract the system natural frequencies for various configurations of the model prior to its being mounted in the wind tunnel.

The first set of impulse tests was designed to extract the uncoupled pitch mode frequency; thus, the plunge degree of freedom was constrained. The model was configured with and without the balsa wood extension and with various amounts of mass ballast during these tests. Data were taken for 16 sec at 64 samples/sec. Overlap averaging of several runs was performed to obtain cleaner data. The results of these experiments are given in table VIII and compared with the analytical predictions based on the finite element model. These results were utilized to verify the mass and stiffness predictions obtained from the finite element model.

Table VIII. Influence of Mass Ballast on the Pitch Frequency

	Analysis	Experiment (uncoupled)
Primary wing	25.78	
With wing extension only	13.29	12.8
Mass ballast, lbm:		
0.005	11.39	10.4
.007	10.86	9.4
.009	10.65	No data
.011	10.41	8.25

A second set of experiments was performed utilizing the impulsive input, which allowed motion in both the plunge and pitch degrees of freedom. Figure 27 shows time histories of hammer input, accelerometer response, and strain gauge output. The power spectral density of the acceleration response (fig. 28(a)) indicates that the natural frequencies of the final configuration are 7.9 and 11.1 Hz. Table IX compares the natural frequencies before and after the actuator elements were added to the finite element model with the experimentally determined values. The structural damping of the plunge mode was also determined from these data by taking the ratio of the frequency width of the peak at the half amplitude and the natural frequency. The damping ratio is half of this value, 0.017. The power spectrum of the strain response (fig. 28(b)) does not define the modes as well; however, the natural frequencies can still be observed from these data.

Free-decay tests. Free-decay tests were used to extract the open loop damping of the pitch mode and to compare the open and closed loop dampings of the plunge mode.

The first set of tests was conducted by constraining the model in plunge and then plucking the pitch spring tine. This method was utilized because the impulse response testing failed to extract data suitable for determining the pitch mode damping. Random input tests could not be used, as there was no actuator for this degree of freedom. The usefulness of this test was limited to determination of the pitch mode damping and frequency because the input signal cannot be recorded. Thus no transfer functions between the input and output can be derived with this method. A resultant time history from the free-decay testing is presented in figure 29. Acceleration response of the open loop system was generated by applying seven impulses during 18 sec. Each response was fully decayed before the next was applied. These data were analyzed with the logarithmic decrement technique, which is detailed in appendix E. The damping ratio ζ, which is half of the structural damping g, was determined to be 0.055.

A similar test was performed on the open and closed loop systems at zero airspeed without the plunge mode being constrained. Although the pitch mode was not constrained either, the model was perturbed by plucking the model at the clamping block, thus primarily exciting the plunge mode. The free-decay results showed damping improvements due to the controller. The strain responses to pluck tests of the open and closed loop systems were compared in figure 30. Both responses were normalized such that
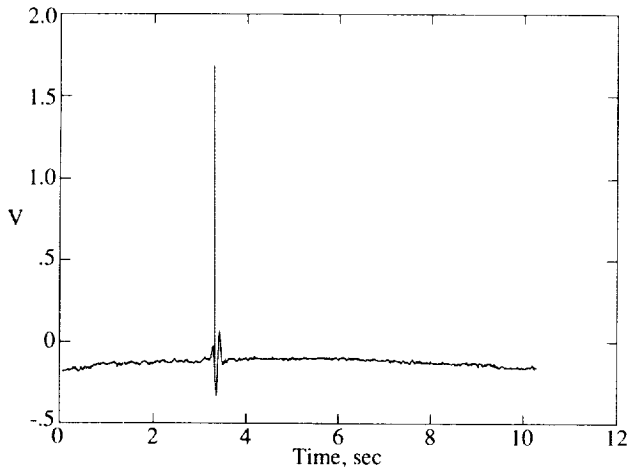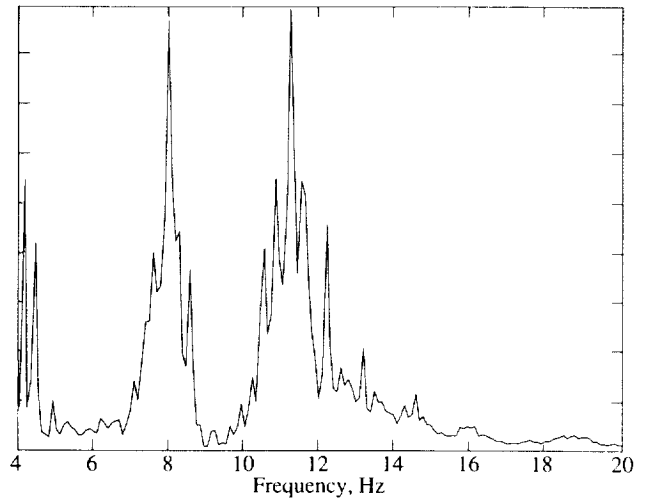
(a) Hammer input.
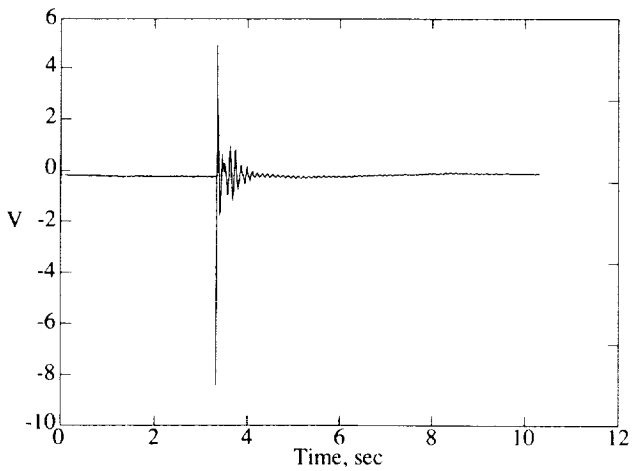
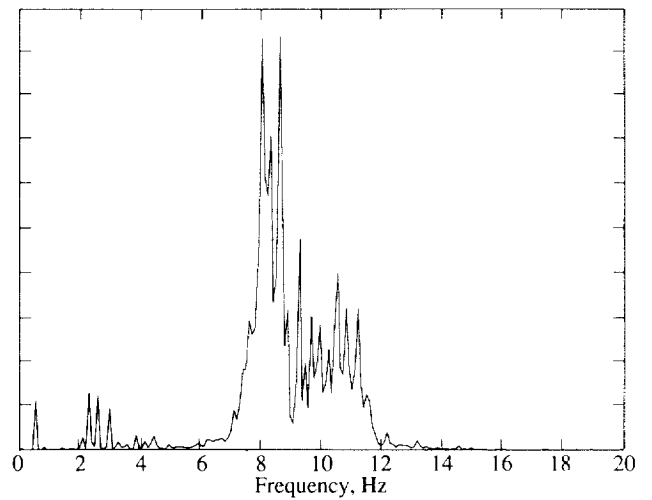(b) Accelerometer output.
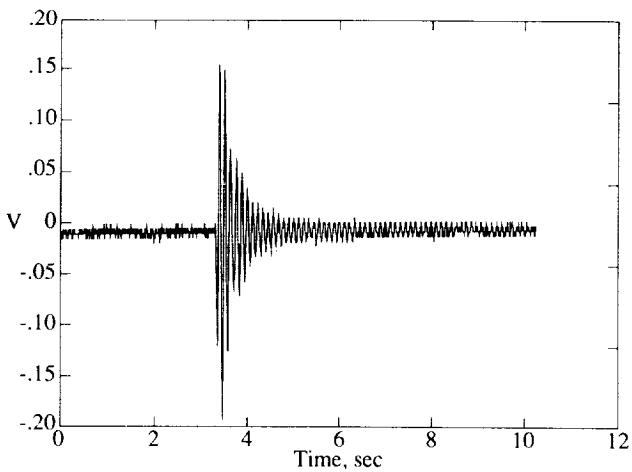
(c) Strain gauge output.

Figure 27. Time histories from hammer tap system identification test.

(a) Normalized power spectral density of acceleration due to hammer.

(b) Normalized power spectral density of strain due to hammer.

Figure 28. Frequency domain analysis of hammer test transfer functions.

Table IX. Natural Frequencies With and Without Piezoelectric Actuators—Analytical and Experimental Results

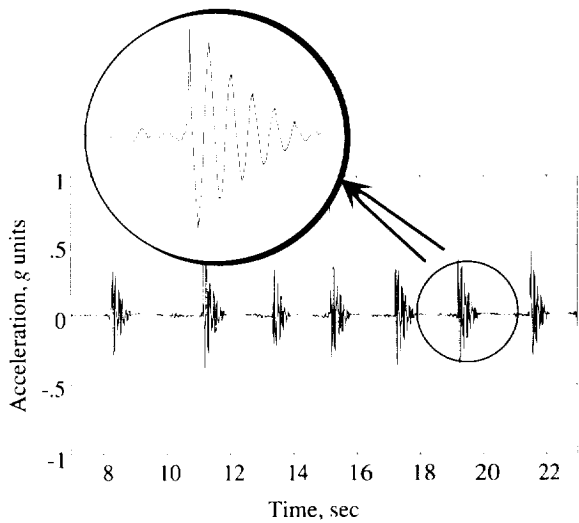|	Plunge mode frequency, Hz	Pitch mode frequency, Hz
Without piezoelectric plates:		
Finite element model	6.8	10.6
Ground vibration test	6.9	12.3
With piezoelectric plates:		
Finite element model	7.8	10.9
System identification	7.9	11.1

24

Figure 29. Time history of acceleration response to plucks at zero airspeed (model constrained in plunge).
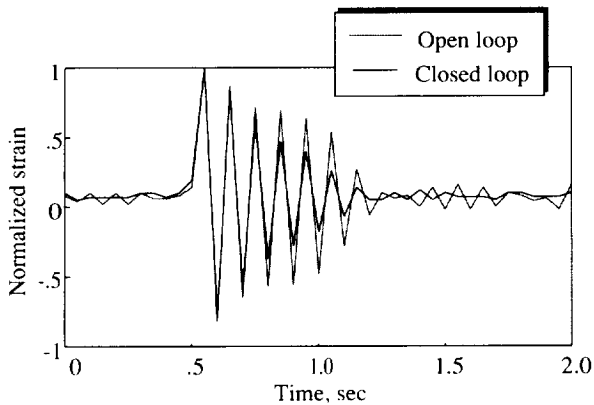

Figure 30. Open and closed loop strain response to free-decay test at zero airspeed.

the magnitude of the first peak was 1.0; the data were obtained by using 20-Hz sample rates. From this plot, the structural damping is shown to have been increased by the presence of the controller.

Random input tests. The open loop system cannot be identified fully with either of the techniques described above because they do not include the influence of the piezoelectric actuator. To obtain system transfer functions, the actuators to be used for control must also be used in the system identification. This criterion was satisfied by tests that input a random signal to the piezoelectric plates. The input signal was random white noise with a Gaussian distribution and a zero mean value. The amplitude of the signal, limited to 3.2 by the operational amplifier,

was adjusted to be as large as possible at the different velocities tested. The larger the signal was, the better the data that were obtained, in terms of coherence. Large excitations near the flutter velocity, however, drove the model unstable.

Random excitations were used to examine open loop behavior as the wind tunnel velocity was increased. Figure 31 shows the magnitude of the strain versus frequency at eight subcritical airspeeds. The plots are dominated by the plunge mode. The sequence of pictures shows that as airspeed is initially increased, the peak magnitude decreases and the width remains fairly constant. Thus, the half magnitude point falls lower on the curve, that is, at a wider point on the peak. Qualitatively this indicates that the damping in this mode increases. At 394 in/sec, the plot shows that the damping is decreasing. The response gets progressively less damped as the flutter speed is approached. This corresponds to trends in the analytical model as shown by the root locus (fig. 21).

Open Loop Flutter Testing

The risks associated with flutter testing are minimized in this experiment by the unique design of the test article. Because the mount system is outside the tunnel and the model is small, it is possible to stop flutter by manually taking hold of the flexible springs or the clamping block.

The flutter tests were conducted by placing the model in the wind tunnel at zero airspeed and then increasing the velocity. Data were taken for several minutes at various airspeeds. During this time interval the model sat at the tunnel condition. Flutter points were defined as the lowest airspeed at which the magnitude of the oscillations diverged within the data-taking interval. The turbulence within the tunnel was relied upon to be sufficient to perturb the model. The increments in velocity were made smaller and data taken more frequently as the speed got near the predicted flutter value. Flutter was encountered experimentally at 580 in/sec; the frequency of the oscillation was 9.4 Hz. A time history of the strain gauge during a run in which flutter was encountered (fig. 32) shows the divergent oscillations that begin growing at 4.5 sec and continue to grow until the maximum possible amplitude is reached at 9.0 sec. At this amplitude, safety stops of the tunnel inhibited the motion of the model so that it would not be destroyed. Frequency domain analysis, performed by taking fast Fourier transforms of the strain time history data, indicates a flutter frequency of 9.4 Hz (fig. 33).
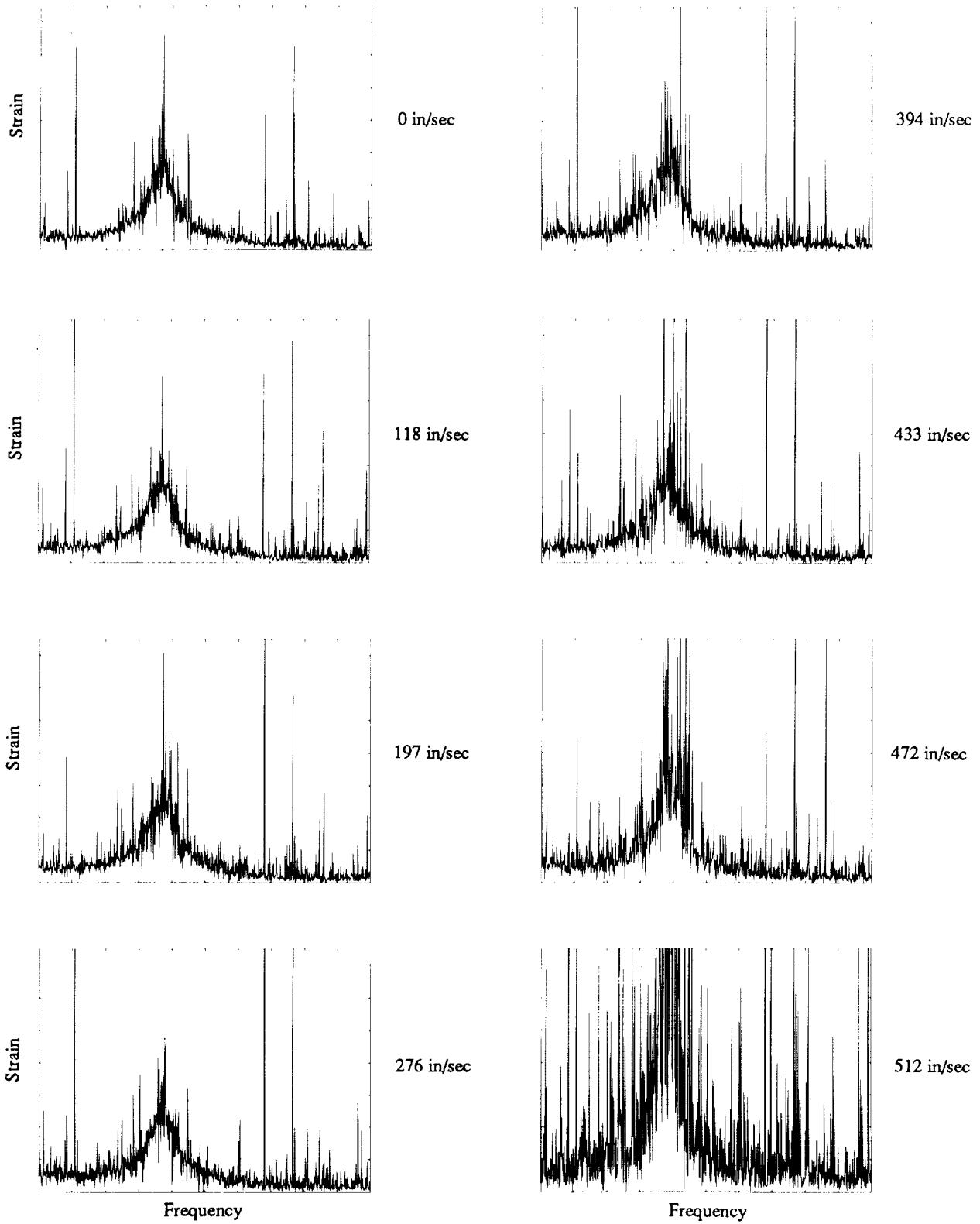
25

Figure 31. Open loop strain magnitude due to random excitations applied through the piezoelectric actuators at various airspeeds.
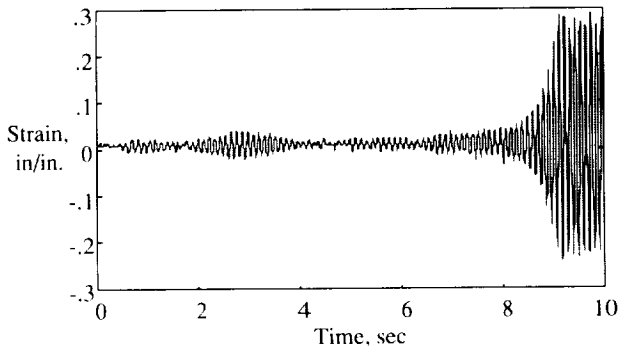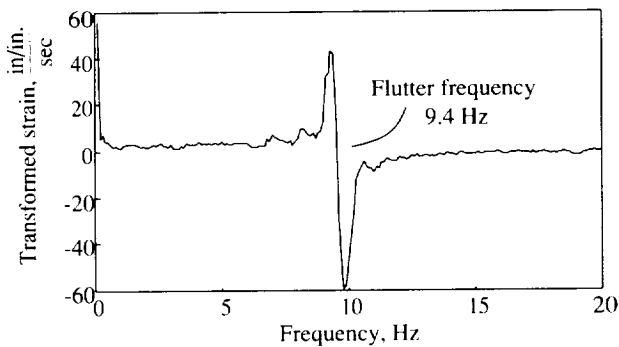
Figure 32. Open loop flutter point; 580 in/sec.

Figure 33. Frequency domain analysis at open loop flutter point; 580 in/sec.

Closed Loop Flutter Testing

The majority of the closed loop flutter testing was initiated by activating the control law at zero airspeed. Proceeding in the same manner as the open loop flutter testing, the speed was increased until flutter was encountered. The closed loop flutter velocity was 697 in/sec at 9.7 Hz.

Increasing airspeed required more control energy to be exerted. As a quantitative indicator of this, the control effort was defined as the sum of the discrete control command signals squared. The control effort expended at several airspeeds is presented in table X. The control effort for this study has been defined as the sum of the absolute values squared of the control computer output. As the velocity increases, the system responses and the control effort increase. The data analyzed at 710 in/sec are actually above the closed loop flutter speed. This is the cause of the dramatic increase in control effort observed. At this velocity, there is not enough control authority to suppress flutter.

The closed loop data were compared with open loop data. Figure 34 shows time histories of the

Table X. Control Effort Expended To Suppress Flutter for Increasing Velocity

Velocity, in/sec	Control effort, V^2
580	122.8
590	172.1
630	196.9
670	228.0
710	*4888.3

*Flutter encountered.

strain response for the two cases. These data were obtained just below the open loop flutter speed, at approximately 575 in/sec. The magnitude of the peaks for the closed loop case is decreased below the magnitude of the open loop peaks. Because of limitations in the controller programming, the controller update rate and data sampling must be consistent. The closed loop data were therefore obtained at a 20-Hz sample rate. The open loop data appear smoother due to a higher sampling rate.

The results of the flutter experiments and analyses are summarized in figure 35. The top graph of figure 35 shows the natural frequency variation as velocity is increased. Examining the zero-airspeed data, the measured open loop values (7.9 and 11.1 Hz) are slightly higher than the analytical predictions of these frequencies (7.8 and 10.9 Hz). The higher frequency mode is the pitch mode; the lower frequency mode is the plunge mode. The analytical values for the two frequencies approach each other as the velocity increases. When frequencies coalesce, flutter generally onsets soon thereafter. The experimental open loop flutter frequency, 9.4 Hz, is slightly larger than the frequency that the analysis predicted for flutter. The final point on this graph is the experimental closed loop flutter frequency, 9.7 Hz.

The lower graph of figure 35 shows the damping ratio variation with velocity. Flutter is indicated on this graph by the damping ratio of one of the modes going to zero. The measured values of damping ratio (0.017 and 0.055) from the zero-airspeed data were utilized in the analytical model. The analysis results are plotted over the velocity range until flutter occurs (i.e., the lower mode crosses the zero-damping axis) at 560 in/sec. This value is 3.5 percent conservative, as the experimental flutter speed was 580 in/sec. The closed loop data at zero airspeed indicate that the control law provided an increase in the damping. Only the data for the plunge mode are presented. Analytical predictions of the damping behavior are
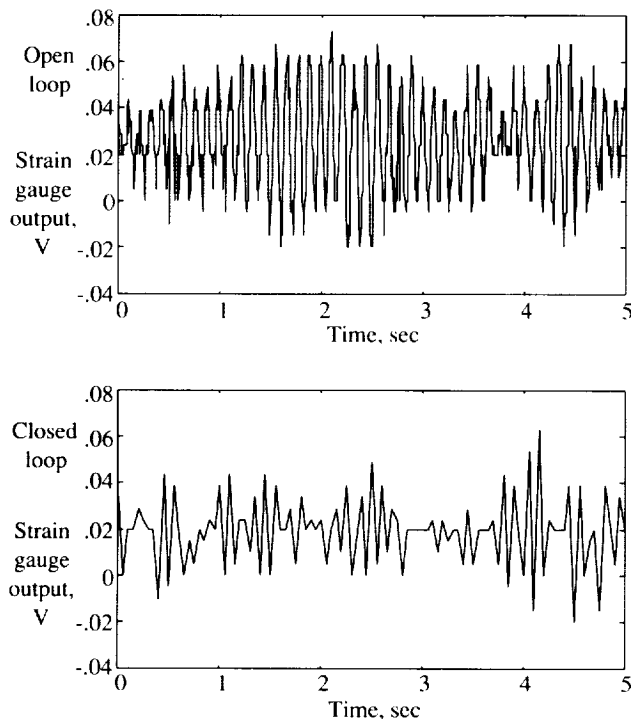
27

Figure 34. Experimental open and closed loop strain response to wind tunnel turbulence just below flutter velocity (575 in/sec).
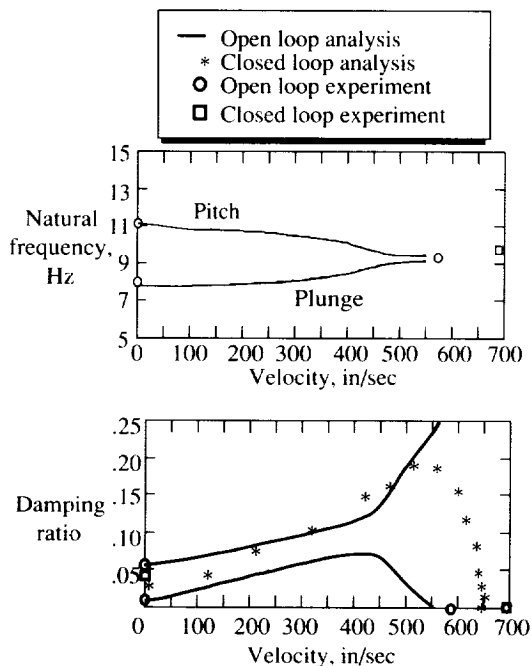

Figure 35. Analytical and experimental flutter results.

presented over the entire velocity range, until closed loop flutter is predicted to occur at 648 in/sec. The

experimental value was 697 in/sec. The predicted value is 7.6 percent conservative. With single-input single-output gain feedback, the flutter speed was predicted to improve by 15.7 percent. The controller actually achieved an improvement of 20 percent in the flutter velocity.

Conclusions and Recommendations

This research effort has resulted in the first experimental demonstration of flutter suppression employing piezoelectric actuators. A wind tunnel model was conceived, designed, fabricated, installed, and tested. Structural and aerodynamic models were created; the aeroservoelastic equations of motion were derived and analyses performed. A digital control law was designed based on a discretized model and was implemented. Open and closed loop flutter tests were conducted, with excellent correlation achieved by analytical predictions.

A two-degree-of-freedom wind tunnel model consisting of a rigid wing attached to a flexible mount system was designed based on preliminary flutter analyses. The rigid wing, with a primary section made of aluminum, was connected to a cantilevered spring tine to control the pitching degree of freedom, and the entire assembly was then connected to a set of spring tines to control the plunging motion. The configuration and dimensions of the model were designed such that it would flutter well within the operating envelope of the tunnel, could be safely tested within the available test section, and would have surfaces suitable for mounting the piezoelectric plates in a bimorph configuration.

Analytical modeling of the wind tunnel model resulted in aeroservoelastic equations of motion. The equations were derived from Lagrange's energy method and utilized modal analysis of a discretized structural model. The natural frequencies were predicted to be 7.8 Hz for the plunge mode and 10.9 Hz for the pitch mode. Generalized aerodynamic forces were generated by the doublet-lattice method and approximated with rational functions. Expressions for the generalized forces associated with the control inputs were derived based on classic laminated plate theory and calculated with finite differencing techniques applied to the discretized structural model results.

Aeroelastic analysis of the open loop system gave a flutter prediction of 560 in/sec. Utilizing the implicit dynamics of the control law computer, a gain feedback control system was designed with strain as the feedback signal. After the gain was optimized for the largest stable velocity range and saturation of the

electronic hardware was accounted for, a gain of 33 was employed. The flutter speed for the closed loop system was predicted to be 648 in/sec, a 15.7-percent increase.

Experimental results from several system identification tests determined the natural frequency of the plunge mode to be 7.9 Hz and that of the pitch mode to be 11.1 Hz. The structural dampings associated with these modes were also determined. The open loop flutter speed was measured at 580 in/sec. The analytical prediction was conservative by 3.5 percent. Closed loop flutter testing was performed and a flutter speed of 697 in/sec was obtained. This represents a 20-percent improvement from the open loop case. The analytical prediction of closed loop flutter speed was conservative by 7.6 percent.

It is recommended that further research be performed in the area of controlling the aeroelastic responses of a vehicle by utilizing piezoelectric actuators. A more realistic and complex model needs to be designed that incorporates strain-actuating elements within the wing design. The concept has been proven to work, however, it has not yet been shown to be viable in terms of real aircraft. Experiments on a larger scale are now called for.

Flutter suppression is not the only aeroelastic application that may call for secondary actuators made of adaptive materials. Load alleviation currently performed by aerodynamic control surfaces may prove to be an ideal application for localized strain actuation. By actuating adaptive material elements, local strains could be produced to counter the loads induced within the structure during maneuvering. This has the potential to extend the service life of aircraft that traditionally undergo high g-loading and to expand operational limits.

The concept of an adaptive material mission-adaptive wing is worthy of investigation. It would eliminate the hydraulic problems encountered on previous attempts to create a wing that can be shape optimized for various flight conditions.

The applications for which adaptive material will be suitable in the future depend heavily on the research in the materials area. Ceramics, which were used in this investigation, are very fragile. Polymers are currently not capable of generating the force levels required for actuating realistic structures. For piezoelectrics to be utilized in aeroelastic applications in an arena beyond research, a more resilient substance than ceramics, or a means to protect the ceramics, needs to be developed.

Appendix A

Parametric Studies for Model Design

During the early stages of model design, sensitivity studies were performed to determine the influences of several key parameters on the flutter characteristics. The baseline structural model was formulated in terms of natural frequencies and a mass matrix. The mode shapes were assumed to be uncoupled rigid body plunge and pitch modes. The mass properties of the wing were specified as those of an isotropic steel plate with the pitch pivot point at the midchord. The mount system stiffnesses for plunging and pitching degrees of freedom were initially chosen such that the natural frequencies were at 9 and 18 Hz, respectively. The baseline aerodynamic model was a rectangular planform with a chord length of 2 in. and a span of 4 in.

The parametric studies were performed on the baseline model by changing the design variables independently and noting the changes in flutter velocity and frequency. Figures A1 through A4 show the resulting trends for variations of the static unbalance, frequency ratio, pitch pivot location, and structural damping. The values on the plots for variation with static unbalance, pitch pivot location, and structural damping have been normalized independently of the others. The flutter velocities on a given plot are divided by the flutter velocity corresponding to the lowest value of the parameter being varied. The flutter frequencies were normalized in the same manner. Thus, on each plot, the value of the left-most point will be 1.0 and apply to both the flutter velocity and the flutter frequency.

Static unbalance is defined by the off-diagonal terms of the symmetric mass matrix. As the static unbalance was increased, the flutter velocity decreased, as shown in figure A1. This is indicative of the additional mass coupling increasing the tendency for modal coalescence. The frequency trend for the same variation showed an increasing frequency. This indicates that the higher frequency mode played a more significant role in the flutter mechanism as the static unbalance term of the mass matrix grew.

The flutter velocity trend with respect to the ratio of frequencies is shown in figure A2. The ratio of frequencies is defined by the plunge frequency divided by the pitch frequency. Note that the increasing ratio represents the distance between the natural frequencies decreasing. Two sets of data are plotted in figure A2. The first set (1) is for various plunging frequencies divided by the baseline value of the pitching frequency, 18 Hz. The graph shows that as
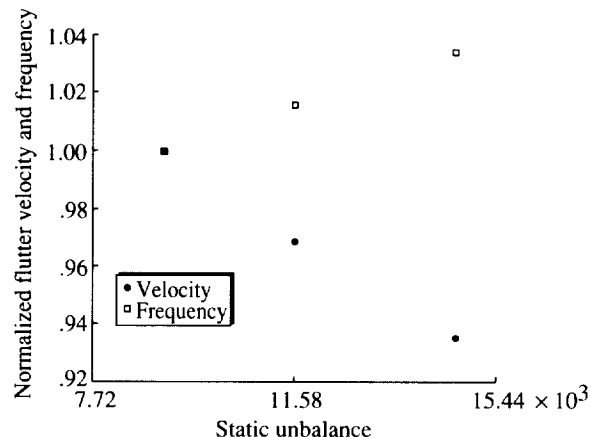
Figure A1. Influence of static unbalance on the flutter velocity and frequency.
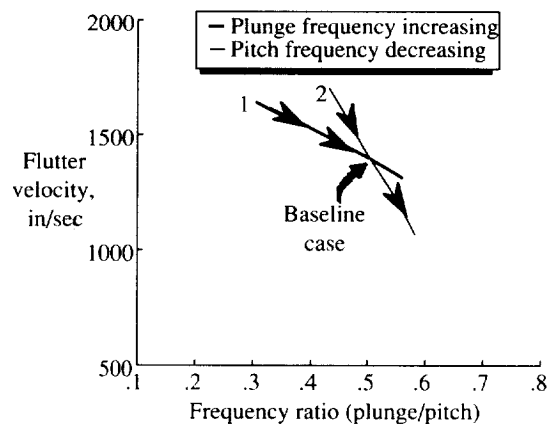
Figure A2. Influence of frequency ratio on the flutter velocity.

the ratio of the frequencies gets larger, the flutter speed decreases. The second set (2) of data is for the baseline value of the plunging frequency, 9 Hz, divided by various values of pitching frequency. The trend is also for the flutter velocity to decrease as this ratio increases. The relative slopes of the two lines indicate that over the range considered, the flutter velocity is more sensitive to reductions in the pitch frequency than to increases in the plunge frequency.

The plot of the pitch pivot location (fig. A3) indicates that as the pivot point is moved toward the trailing edge of the wing, the flutter velocity is lowered. Recalling that for these variations the center of gravity was located at the midchord, or 1.0, locations aft of 1.0 are for statically unstable wings. Long before flutter, divergence will have occurred.
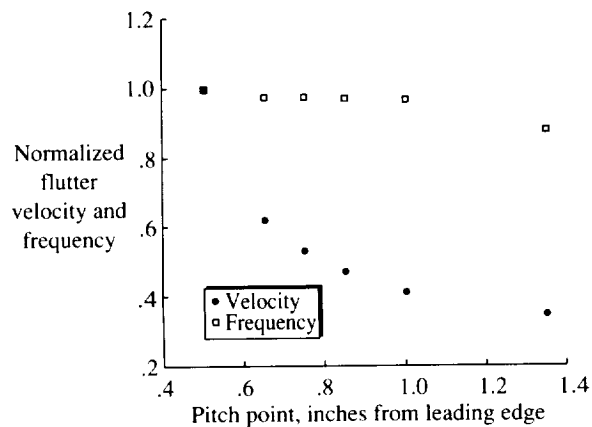
Figure A3. Influence of pitch pivot location on the flutter velocity and frequency.

Figure A4 shows the change in flutter velocity and frequency as the structural damping is increased simultaneously in both the plunge and the pitch modes. The trends show that the velocity increases, as expected, since the eigenvalues at zero airspeed will be farther from the instability point (i.e., the modes are more stable). The trend is not linear, but for low values, each percent of additional structural damping raises the velocity by roughly a percent. The

frequency of flutter is shown to decrease as structural damping is added. The addition of structural damping lowers values of damped frequencies and brings them closer together, predictably lowering the flutter frequency.
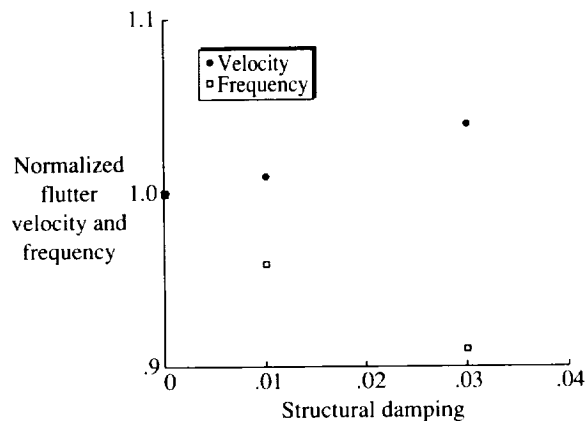
Figure A4. Influence of structural damping on the flutter velocity and frequency.

Changes to the design based on the trends seen in these parametric variations greatly reduced the number of iterations required in arriving at a final configuration.

Appendix B

Equations of Motion for Aeroelastic Systems Utilizing Laminated Plate Theory

This appendix describes the derivation of Lagrange's equations of motion for an aeroelastic system controlled by piezoelectric actuators. The equations derived in appendix D are utilized for the calculation of the actuator components of the equations. The constitutive relations developed in appendix C are also incorporated into the potential energy equation.

Lagrange's equations of motion require the derivation of expressions for potential and kinetic energy as functions of generalized coordinates. The aeroelastic modeling was performed with the orthogonal or undamped modes of vibration as the generalized coordinates.

Plate displacements may be expressed in terms of these coordinates:

$$u\left(x, y, z, t\right) = \sum_{i=1}^{L} \mathbf{\Psi}_{xi}\left(x_i, y_i, z_i\right) q_{xi}\left(t\right) \tag{B1}$$

$$v\left(x, y, z, t\right) = \sum_{i=1}^{M} \mathbf{\Psi}_{yi}\left(x_i, y_i, z_i\right) q_{yi}\left(t\right) \tag{B2}$$

$$w\left(x, y, z, t\right) = \sum_{i=1}^{N} \mathbf{\Psi}_{zi}\left(x_i, y_i, z_i\right) q_{zi}\left(t\right) \tag{B3}$$

where $\mathbf{\Psi}_{(x,y,z)i}$ are the mode shape vectors in the x-, y-, and z-directions, respectively, and $q_{(x,y,z)i}(t)$ are time-dependent generalized coordinates. The x-translation, u, of the system at the (x_0, y_0, z_0) location is expressed as

$$u\left(x_0, y_0, z_0\right) = \mathbf{\Psi}_{x1}\left(x_0, y_0, z_0\right) q_{x1} + \mathbf{\Psi}_{x2}\left(x_0, y_0, z_0\right) q_{x2} + \ldots \tag{B4}$$

In matrix notation, the translational degrees of freedom are written

$$\left\{\begin{array}{c} u \\ v \\ w \end{array}\right\} = \mathbf{\Psi} \mathbf{q} \tag{B5}$$

where

$$\mathbf{\Psi} = \begin{bmatrix} \mathbf{\Psi}_{x1}, \mathbf{\Psi}_{x2}, \ldots, \mathbf{\Psi}_{xL} & 0 & 0 \\ 0 & \mathbf{\Psi}_{y1}, \mathbf{\Psi}_{y2}, \ldots, \mathbf{\Psi}_{yM} & 0 \\ 0 & 0 & \mathbf{\Psi}_{z1}, \mathbf{\Psi}_{z2}, \ldots, \mathbf{\Psi}_{zN} \end{bmatrix} \tag{B6}$$

and

$$\mathbf{q}^T = \left\{ q_{x1} \ q_{x2} \cdots q_{xL} \vdots q_{y1} \ q_{y2} \cdots q_{yM} \vdots q_{z1} \ q_{z2} \cdots q_{zN} \right\} \tag{B7}$$

The potential energy of the system is defined as

$$U = \frac{1}{2} \iiint_{\text{Volume}} \{\varepsilon\}^T \{\sigma\} \, dV \tag{B8}$$

The constitutive equations, detailed in appendix C, provide the relationship between the stress and the strain:

$$\boldsymbol{\sigma} = \mathbf{G}\left(\boldsymbol{\varepsilon} - \boldsymbol{\Lambda}\right) \tag{B9}$$

The total strain ε can be calculated based on midplane strain ε_0 and curvature κ. The longitudinal and lateral strains and the shear strain are defined as

$$\varepsilon_{xx} = \frac{\partial u}{\partial x} \tag{B10}$$

$$\varepsilon_{yy} = \frac{\partial v}{\partial y} \tag{B11}$$

$$\gamma_{xy} = \frac{\partial u}{\partial y} + \frac{\partial v}{\partial x} \tag{B12}$$

For a plate, the displacements are related to quantities at the midplane (midplane denoted by the subscript 0):

$$u = u_0 - z\frac{\partial w_0}{\partial x} \tag{B13}$$

$$v = v_0 - z\frac{\partial w_0}{\partial y} \tag{B14}$$

$$w = w_0 \tag{B15}$$

which allows the plate strains to be expressed as

$$\varepsilon_{xx} = \frac{\partial u_0}{\partial x} - z\frac{\partial^2 w_0}{\partial x^2} \tag{B16}$$

$$\varepsilon_{yy} = \frac{\partial v_0}{\partial y} - z\frac{\partial^2 w_0}{\partial^2 y} \tag{B17}$$

$$\gamma_{xy} = \frac{\partial u_0}{\partial y} + \frac{\partial v_0}{\partial x} - 2z\frac{\partial^2 w_0}{\partial x\,\partial y} \tag{B18}$$

or

$$\varepsilon_{xx} = \varepsilon_{xx_0} + z\kappa_x \tag{B19}$$

$$\varepsilon_{yy} = \varepsilon_{yy_0} + z\kappa_y \tag{B20}$$

$$\gamma_{xy} = \gamma_{xy_0} + z\kappa_{xy} \tag{B21}$$

where the following definitions are made:

$$\varepsilon_{xx_0} = \frac{\partial u_0}{\partial x} \tag{B22}$$

$$\varepsilon_{yy_0} = \frac{\partial v_0}{\partial y} \tag{B23}$$

$$\gamma_{xy} = \frac{\partial u_0}{\partial y} + \frac{\partial v_0}{\partial x} \tag{B24}$$

$$\kappa_x = -\frac{\partial^2 w_0}{\partial x^2} \tag{B25}$$

$$\kappa_y = -\frac{\partial^2 w_0}{\partial y^2} \tag{B26}$$

$$\kappa_{xy} = -2\frac{\partial^2 w_0}{\partial x\,\partial y} \tag{B27}$$

Strain, expressed as

$$\varepsilon = \varepsilon_0 + z\kappa \tag{B28}$$

is substituted into the constitutive equations to provide

$$\sigma = \mathbf{G}\left(\varepsilon_0 + z\kappa - \boldsymbol{\Lambda}\right) \tag{B29}$$

The potential energy now becomes

$$U = \frac{1}{2} \iiint\limits_{\text{Volume}} \left(\varepsilon_0 + z\kappa\right)^T \mathbf{G}\left(\varepsilon_0 + z\kappa - \boldsymbol{\Lambda}\right) dV \tag{B30}$$

$$U = \frac{1}{2} \iiint\limits_{\text{Volume}} \left(\varepsilon_0 + z\kappa\right)^T \mathbf{G}\left(\varepsilon_0 + z\kappa\right) dV - \frac{1}{2} \iiint\limits_{\text{Volume}} \left(\varepsilon_0 + z\kappa\right)^T \mathbf{G}\left\{\boldsymbol{\Lambda}\right\} dV \tag{B31}$$

Note that the midplane strain and the curvature are independent of z. Thus,

$$\iiint\limits_{\text{Volume}} dV = \iint\limits_{\text{Area}} \int\limits_{\text{Thickness}} dz\, dA \tag{B32}$$

The potential energy can then be calculated:

$$U = \frac{1}{2} \iint\limits_{\text{Area}} \varepsilon_0{}^T \left[\int\limits_{\text{Thickness}} \mathbf{G}\, dz\right] \varepsilon_0 + \varepsilon_0{}^T \left[\int\limits_{\text{Thickness}} \mathbf{G}z\, dz\right] \kappa + \kappa^T \left[\int\limits_{\text{Thickness}} \mathbf{G}z\, dz\right] \varepsilon_0$$

$$+ \kappa^T \left[\int\limits_{\text{Thickness}} \mathbf{G}z^2\, dz\right] \kappa\, dA - \frac{1}{2} \iint\limits_{\text{Area}} \varepsilon_0{}^T \left[\int\limits_{\text{Thickness}} \mathbf{G}\boldsymbol{\Lambda}\, dz\right] + \kappa^T \left[\int\limits_{\text{Thickness}} \mathbf{G}z\boldsymbol{\Lambda}\, dz\right] dA \tag{B33}$$

The integrals through the thickness are defined as:

$$\boldsymbol{A} = \int\limits_{\text{Thickness}} \mathbf{G}\, dz \tag{B34}$$

$$\boldsymbol{B} = \int\limits_{\text{Thickness}} \mathbf{G}z\, dz \tag{B35}$$

$$\boldsymbol{D} = \int\limits_{\text{Thickness}} \mathbf{G}z^2\, dz \tag{B36}$$

$$\boldsymbol{N_\Lambda} = \int\limits_{\text{Thickness}} \mathbf{G}\boldsymbol{\Lambda}\, dz \tag{B37}$$

$$\boldsymbol{M_\Lambda} = \int\limits_{\text{Thickness}} \mathbf{G}z\boldsymbol{\Lambda}\, dz \tag{B38}$$

The $\boldsymbol{A}$, $\boldsymbol{B}$, and $\boldsymbol{D}$ matrices are called extensional, coupling, and bending stiffnesses, respectively.

34

The potential energy, expressed in terms of these integrals, is written

$$U = \frac{1}{2} \iint\limits_{\text{Area}} \varepsilon_0{}^T A \varepsilon_0 + \varepsilon_0{}^T B \kappa + \kappa^T B \varepsilon_0 + \kappa^T D \kappa \, dA - \frac{1}{2} \iint\limits_{\text{Area}} \varepsilon_0{}^T N_\Lambda + \kappa^T M_\Lambda \, dA \tag{B39}$$

or

$$U = \frac{1}{2} \iint\limits_{\text{Area}} \left\{ \varepsilon_0{}^T \quad \kappa^T \right\} \begin{bmatrix} A & B \\ B & D \end{bmatrix} \left\{ \begin{array}{c} \varepsilon_0 \\ \kappa \end{array} \right\} dA - \frac{1}{2} \iint\limits_{\text{Area}} \left\{ \varepsilon_0{}^T \quad \kappa^T \right\} \left\{ \begin{array}{c} N_\Lambda \\ M_\Lambda \end{array} \right\} dA \tag{B40}$$

Referring back to the strain and curvature functions in terms of displacements, an operator $\mathcal{D}$ is defined such that

$$\left\{ \begin{array}{c} \varepsilon_0 \\ \kappa \end{array} \right\} = [\mathcal{D}] \left\{ \begin{array}{c} u_0 \\ v_0 \\ w_0 \end{array} \right\} \tag{B41}$$

where

$$[\mathcal{D}]^T = \begin{bmatrix} \frac{\partial}{\partial x} & 0 & \frac{\partial}{\partial y} & 0 & 0 & 0 \\ 0 & \frac{\partial}{\partial y} & \frac{\partial}{\partial x} & 0 & 0 & 0 \\ 0 & 0 & 0 & -\frac{\partial^2}{\partial x^2} & -\frac{\partial^2}{\partial y^2} & -2\frac{\partial^2}{\partial x \, \partial y} \end{bmatrix} \tag{B42}$$

The general relation from midplane displacements to displacements at a distance z from the midplane is easily derived. However, if the displacements are given for the midplane, as is the case for plate element results of a finite element model, there is a one-to-one correspondence. The subscripts on the displacement vector are thus dropped.

Recalling the expression for the displacements in terms of generalized coordinates allows the midplane strain and curvature to be expressed:

$$\left\{ \begin{array}{c} \varepsilon_0 \\ \kappa \end{array} \right\} = [\mathcal{D}] [\Psi] \, \mathbf{q}(t) \tag{B43}$$

Substituting this expression into the potential energy expression,

$$U = \frac{1}{2} \iint\limits_{\text{Area}} \mathbf{q}^T \Psi^T \mathcal{D}^T \begin{bmatrix} A & B \\ B & D \end{bmatrix} \mathcal{D} \Psi \mathbf{q} \, dA - \frac{1}{2} \iint\limits_{\text{Area}} \mathbf{q}^T \Psi^T \mathcal{D}^T \left\{ \begin{array}{c} N_\Lambda \\ M_\Lambda \end{array} \right\} dA \tag{B44}$$

or, moving the generalized coordinate outside the integrals

$$U = \frac{1}{2} \mathbf{q}^T \mathbf{F}_1 \mathbf{q} - \frac{1}{2} \mathbf{q}^T \mathbf{F}_2 \tag{B45}$$

where

$$\mathbf{F}_1 = \iint\limits_{\text{Area}} [\mathcal{D}\Psi]^T \begin{bmatrix} A & B \\ B & D \end{bmatrix} [\mathcal{D}\Psi] \, dA \tag{B46}$$

$$\mathbf{F}_2 = \iint\limits_{\text{Area}} [\mathcal{D}\Psi]^T \left\{ \begin{array}{c} N_\Lambda \\ M_\Lambda \end{array} \right\} dA \tag{B47}$$

$\mathbf{F}_1$ is the generalized structural stiffness matrix $\mathbf{K}_s$.

The kinetic energy development follows a similar path. By definition, kinetic energy T is

$$T = \frac{1}{2} \iiint\limits_{\text{Volume}} \rho \{\dot{u}\}^T \{\dot{u}\} \, dV \tag{B48}$$

where

$$\{u\} = \left\{ \begin{array}{c} u \\ v \\ w \end{array} \right\} \tag{B49}$$

From equation (B5), the displacement vector is expressed by the mode shapes multiplied by the generalized coordinates. The mode shapes are independent of time, so that the expression for the time derivative of displacement is

$$\{\dot{u}\} = [\boldsymbol{\Psi}] \{\dot{q}\} \tag{B50}$$

where (˙) represents the derivative with respect to time. The kinetic energy is then written

$$T = \frac{1}{2} \iiint\limits_{\text{Volume}} \rho \dot{q}^T \boldsymbol{\Psi}^T \boldsymbol{\Psi} \dot{q} \, dV \tag{B51}$$

Moving the generalized coordinates outside the integral, the expression becomes

$$T = \frac{1}{2} \dot{q}^T \iiint\limits_{\text{Volume}} \rho \boldsymbol{\Psi}^T \boldsymbol{\Psi} \, dV \, \dot{q} \tag{B52}$$

or

$$T = \frac{1}{2} \dot{q}^T \mathbf{F}_3 \dot{q} \tag{B53}$$

where

$$\mathbf{F}_3 = \iiint\limits_{\text{Volume}} \rho \boldsymbol{\Psi}^T \boldsymbol{\Psi} \, dV \tag{B54}$$

The triple integral over the volume can be expressed as the double integral over the area of the integral over the thickness. Assuming that the mode shapes are constant through the thickness, the mass per unit area, m_0, is defined as the integral of the density through the thickness. The expression for $\mathbf{F}_3$ is recognized as the generalized structural mass matrix:

$$\mathbf{M}_s = \mathbf{F}_3 = \iint\limits_{\text{Area}} m_0 \boldsymbol{\Psi}^T \boldsymbol{\Psi} \, dA \tag{B55}$$

In formulating the Lagrangian equations of motion, the conservative forces of the system are contained in the potential and kinetic energy expressions (ref. 33). The nonconservative forces, namely the aerodynamics, are represented by generalized forces $\mathbf{Q}_i$:

$$\frac{d}{dt} \left(\frac{\partial T}{\partial q_i} \right) - \frac{\partial T}{\partial q_i} + \frac{\partial U}{\partial q_i} + \frac{\partial \mathbf{D}}{\partial \dot{q}_i} = \mathbf{Q}_i \tag{B56}$$

From the previously derived energy expressions, the Lagrange equations become

$$\mathbf{F}_3 \ddot{q} + \frac{\partial \mathbf{D}}{\partial \dot{q}_i} + \mathbf{F}_1 q = \mathbf{Q}_i + \mathbf{F}_2 \tag{B57}$$

which can be transformed to the Laplace domain and rewritten as

$$\left(\mathbf{M}_s s^2 + \mathbf{D}_s s + \mathbf{K}_s \right) \{q_f\} + \bar{q} [\mathbf{Q}_f] \{q_f\} = \mathbf{F}_2 \tag{B58}$$

This is the classical second order aeroelastic equation formulation with the exception of the term on the right-hand side; $\mathbf{F}_2$ is the force generated by the actuating strain, which arose from the addition to the potential energy expression. It appeared because a mechanical stress was being produced by a nonmechanical strain. In the aeroelastic problem, Lagrange's equations are written as a balance of mechanical energy. Further development of the strain actuation matrix is presented in appendix D.

In order to transform the aerodynamics into the Laplace domain, it was necessary to apply a second order rational function approximation to the aerodynamics (ref. 34):

$$\mathbf{Q}_f \cong \widehat{\mathbf{Q}}_f = \left[\widehat{\mathbf{A}}_0\right]_f + \left[\widehat{\mathbf{A}}_1\right]_f s\left(\frac{c}{2\mathrm{v}}\right) + \left[\widehat{\mathbf{A}}_2\right]_f s^2\left(\frac{c}{2\mathrm{v}}\right)^2 \tag{B59}$$

Equation (B58) is then expressed

$$\left(\widetilde{\mathbf{M}}s^2 + \widetilde{\mathbf{D}}s + \widetilde{\mathbf{K}}\right)\{\mathbf{q}_f\} = \mathbf{F}_2 \tag{B60}$$

where

$$\widetilde{\mathbf{K}} = \mathbf{K}_s + \bar{q}\left[\widehat{\mathbf{A}}_0\right]_f \tag{B61}$$

$$\widetilde{\mathbf{D}} = \mathbf{D}_s + \bar{q}\left(\frac{c}{2\mathrm{v}}\right)\left[\widehat{\mathbf{A}}_1\right]_f \tag{B62}$$

$$\widetilde{\mathbf{M}} = \mathbf{M}_s + \bar{q}\left(\frac{c}{2\mathrm{v}}\right)^2\left[\widehat{\mathbf{A}}_2\right]_f \tag{B63}$$

Defining the vectors

$$x_{f_1} = \{\mathbf{q}_f\} \tag{B64}$$

$$x_{f_2} = s\{\mathbf{q}_f\} \tag{B65}$$

these equations can be readily converted to first order form (ref. 35):

$$s\left\{\begin{array}{c} x_{f_1} \\ x_{f_2} \end{array}\right\} = \left[\begin{array}{cc} 0 & I \\ -\widetilde{\mathbf{M}}^{-1}\widetilde{\mathbf{K}} & -\widetilde{\mathbf{M}}^{-1}\widetilde{\mathbf{D}} \end{array}\right]\left\{\begin{array}{c} x_{f_1} \\ x_{f_2} \end{array}\right\} + \left\{\begin{array}{c} 0 \\ -\widetilde{\mathbf{M}}^{-1}\mathbf{F}_2 \end{array}\right\} \tag{B66}$$

From the development of the strain actuation matrix in appendix D, the aeroservoelastic equations of motion are expressed as:

$$s\left\{\begin{array}{c} x_{f_1} \\ x_{f_2} \end{array}\right\} = \left[\begin{array}{cc} 0 & I \\ -\widetilde{\mathbf{M}}^{-1}\widetilde{\mathbf{K}} & -\widetilde{\mathbf{M}}^{-1}\widetilde{\mathbf{D}} \end{array}\right]\left\{\begin{array}{c} x_{f_1} \\ x_{f_2} \end{array}\right\} + \left\{\begin{array}{c} 0 \\ -\widetilde{\mathbf{M}}^{-1}\Gamma d_{31} \end{array}\right\}\mathbf{V}_3 \tag{B67}$$

In traditional controls notation (ref. 30),

$$\dot{\mathbf{x}} = \mathbf{A}\mathbf{x} + \mathbf{B}\mathbf{u} \tag{B68}$$

Appendix C

Development of the Constitutive Relations for a Piezoelectric Material

This appendix develops the constitutive equations for a piezoelectric material, taking them from the generalized Hooke's law to a subset utilized in laminated plate theory and expressed in a form useful in the derivation of the potential energy equation.

Mechanical stresses and strains are related through a 6 by 6 compliance matrix in the generalized Hooke's law. The constitutive relations for a linear elastic material with three mutually perpendicular planes of elastic symmetry have nine independent entries in the compliance matrix. Classic laminated plate theory (ref. 35) is used in developing the equations, so only the in-plane stresses and strains are considered, reducing the independent elements to four, as shown in the following equation:

$$
\begin{Bmatrix} \varepsilon_{xx} \\ \varepsilon_{yy} \\ \gamma_{xy} \end{Bmatrix} = \begin{bmatrix} \frac{1}{E_1} & -\frac{\nu_{21}}{E_2} & 0 \\ -\frac{\nu_{12}}{E_1} & \frac{1}{E_2} & 0 \\ 0 & 0 & \frac{1}{G_{12}} \end{bmatrix} \begin{Bmatrix} \sigma_x \\ \sigma_y \\ \tau_{xy} \end{Bmatrix} \quad (C1)
$$

which can be expressed as

$$
\varepsilon = \mathbf{S}\,\sigma \quad (C2)
$$

The strain vector ε and the stress vector σ are related by the compliance matrix $\mathbf{S}$. An alternate method of expressing this relationship is through a stiffness matrix $\mathbf{G}$:

$$
\sigma = \mathbf{G}\varepsilon \quad (C3)
$$

The electrical quantities (flux density $\mathbf{R}$ and voltage per thickness $\mathbf{E}$) are related by the dielectric equations through permittivity β and impermittivity ϵ matrices (ref. 7):

$$
\mathbf{E} = \beta\mathbf{R} \quad (C4)
$$

$$
\mathbf{R} = \epsilon\mathbf{E} \quad (C5)
$$

where

$$
\mathbf{E} = \frac{\mathbf{V}}{t} \quad (C6)
$$

For piezoelectric systems, the coupling of the two fields is accomplished by the introduction of the strain-charge matrix:

$$
\varepsilon = \mathbf{S}\,\sigma + \mathbf{d}^{\mathrm{T}}\mathbf{E} \quad (C7)
$$

The nonzero terms for a PZT plate with poling in the 3-direction are

$$
[\mathbf{d}] = \begin{bmatrix} 0 & 0 & 0 & 0 & d_{15} & 0 \\ 0 & 0 & 0 & d_{24} & 0 & 0 \\ d_{31} & d_{32} & d_{33} & 0 & 0 & 0 \end{bmatrix} \quad (C8)
$$

Once again, by using classic laminated plate theory, this matrix reduces to a 3 by 3:

$$
\mathbf{d} = \begin{bmatrix} 0 & 0 & d_{15} \\ 0 & 0 & 0 \\ d_{31} & d_{32} & 0 \end{bmatrix} \quad (C9)
$$

When the electrodes are on the faces of the plate perpendicular to the poling direction, the only voltage that can be applied is in the 3-direction. Therefore,

$$
\mathbf{E} = \begin{Bmatrix} 0 \\ 0 \\ E_3 \end{Bmatrix} \quad (C10)
$$

Defining Λ as the actuation strain vector leads to

$$
\Lambda = \begin{Bmatrix} \Lambda_1 \\ \Lambda_2 \\ \Lambda_3 \end{Bmatrix} = \mathbf{d}^{\mathrm{T}}\mathbf{E} = \begin{Bmatrix} d_{31} \\ d_{32} \\ 0 \end{Bmatrix} E_3 \quad (C11)
$$

Solving equation (D6) for the stress vector, and defining $\mathbf{G}$ as the inverse of the compliance matrix,

$$
\sigma = \mathbf{G}\,(\varepsilon - \Lambda) \quad (C12)
$$

where

$$
\mathbf{G} = \begin{bmatrix} \frac{E_1}{1 - \nu_{12}\nu_{21}} & \frac{\nu_{21}E_2}{1 - \nu_{12}\nu_{21}} & 0 \\ \frac{\nu_{12}E_2}{1 - \nu_{12}\nu_{21}} & \frac{E_2}{1 - \nu_{12}\nu_{21}} & 0 \\ 0 & 0 & G_{12} \end{bmatrix} \quad (C13)
$$

Note that use of the laminar plate model neglects any influence of the d_{33} coefficient and that applying the voltage parallel to the polarization negates the influence of the d_{15} coefficient.

Appendix D

Analytical Modeling of the Piezoelectric Actuator

The equations derived in appendix B consist of components that are calculated by standard methods, with the exception of the force due to the piezoelectric actuators $\mathbf{F}_2$. This appendix presents a more detailed look at the calculation of this matrix, as well as the approximations used to implement the calculations.

From equation (B47), the force is given as

$$\mathbf{F}_2 = \iint\limits_{\text{Area}} [\mathcal{D}\boldsymbol{\Psi}]^T \left\{ \begin{array}{c} \boldsymbol{M}_\Lambda \\ \boldsymbol{N}_\Lambda \end{array} \right\} dA \qquad (D1)$$

The rows of the force and moment due to strain actuation may be specified

$$\boldsymbol{N}_\Lambda = \left\{ \begin{array}{c} N_{\Lambda_1} \\ N_{\Lambda_2} \\ N_{\Lambda_3} \end{array} \right\} \qquad (D2)$$

$$\boldsymbol{M}_\Lambda = \left\{ \begin{array}{c} M_{\Lambda_1} \\ M_{\Lambda_2} \\ M_{\Lambda_3} \end{array} \right\} \qquad (D3)$$

The definitions of the operator and modal matrices are recalled from equations (B6) and (B42):

$$[\mathcal{D}\boldsymbol{\Psi}] = \begin{bmatrix} \frac{\partial}{\partial x} & 0 & 0 \\ 0 & \frac{\partial}{\partial y} & 0 \\ \frac{\partial}{\partial y} & \frac{\partial}{\partial x} & 0 \\ 0 & 0 & -\frac{\partial^2}{\partial x^2} \\ 0 & 0 & -\frac{\partial^2}{\partial y^2} \\ 0 & 0 & -2\frac{\partial^2}{\partial x\,\partial y} \end{bmatrix} \begin{bmatrix} [\boldsymbol{\Psi}_{x_i}] & 0 & 0 \\ 0 & [\boldsymbol{\Psi}_{y_i}] & 0 \\ 0 & 0 & [\boldsymbol{\Psi}_{z_i}] \end{bmatrix}$$
$$(D4)$$

Consider only the out-of-plane displacements (i.e., $\boldsymbol{\Psi}_{x_i}$ and $\boldsymbol{\Psi}_{y_i}$ are zero); the matrix dimension shrinks to

$$[\mathcal{D}\boldsymbol{\Psi}]^T = \begin{bmatrix} 0 & 0 & 0 & -\frac{\partial^2 \boldsymbol{\Psi}_z}{\partial x^2} & -\frac{\partial^2 \boldsymbol{\Psi}_z}{\partial y^2} & -2\frac{\partial^2 \boldsymbol{\Psi}_z}{\partial x\,\partial y} \end{bmatrix} \quad (D5)$$

In the design of the flexible mount system, special consideration was given to preventing the plunge spring tines from deforming in torsion. The piezoelectric plates are oriented along the spring tines, which deform primarily in the y-direction (i.e., creating moments about the x-axis). Therefore any

derivative taken with respect to x will be considered negligible, leaving

$$[\mathcal{D}\boldsymbol{\Psi}]^T = \begin{bmatrix} 0 & 0 & 0 & 0 & -\frac{\partial^2 \boldsymbol{\Psi}_z}{\partial y^2} & 0 \end{bmatrix} \qquad (D6)$$

Thus,

$$\mathbf{F}_2 = \int\limits_{\text{Area}} \left(-\frac{\partial^2 \boldsymbol{\Psi}_z}{\partial y^2} \right) M_{\Lambda_2}\, dA \qquad (D7)$$

The piezoelectrically induced moment was derived in equation (B38):

$$\boldsymbol{M}_\Lambda = \int\limits_{\text{Thickness}} \mathbf{G}z\boldsymbol{\Lambda}\, dz \qquad (D8)$$

The second row, corresponding to M_{Λ_2}, is

$$M_{\Lambda_2} = \int\limits_{\text{Thickness}} \left[\frac{\nu_{12}E_{12}}{1-\nu_{12}\nu_{21}} \quad \frac{E_2}{1-\nu_{12}\nu_{21}} \quad 0 \right] \left\{ \begin{array}{c} \Lambda_1 \\ \Lambda_2 \\ 0 \end{array} \right\} z\, dz \quad (D9)$$

Recall from the discussion of constitutive relations that

$$\left\{ \begin{array}{c} \Lambda_1 \\ \Lambda_2 \\ 0 \end{array} \right\} = \left\{ \begin{array}{c} 1 \\ 1 \\ 0 \end{array} \right\} d_{31}\frac{\mathrm{V}_3}{\mathrm{t}} \qquad (D10)$$

Then

$$M_{\Lambda_2} = \int\limits_{\text{Thickness}} \left(\frac{\nu_{12}+1}{1-\nu_{12}\nu_{21}} \right) E_2 d_{31}\frac{1}{\mathrm{t}}\mathrm{V}_3 z\, dz \qquad (D11)$$

Defining

$$\gamma = \left(\frac{\nu_{12}+1}{1-\nu_{12}\nu_{21}} \right) E_2 d_{31}\frac{1}{\mathrm{t}} \qquad (D12)$$

provides

$$M_{\Lambda_2} = \int\limits_{\text{Thickness}} \gamma \mathrm{V}_3 z\, dz \qquad (D13)$$

The scalar γ consists of geometric and material properties. For any isotropic lamina, γ is independent of the location z, so it may be taken outside the integral. The structure is considered to consist of several layers composed of different materials. The
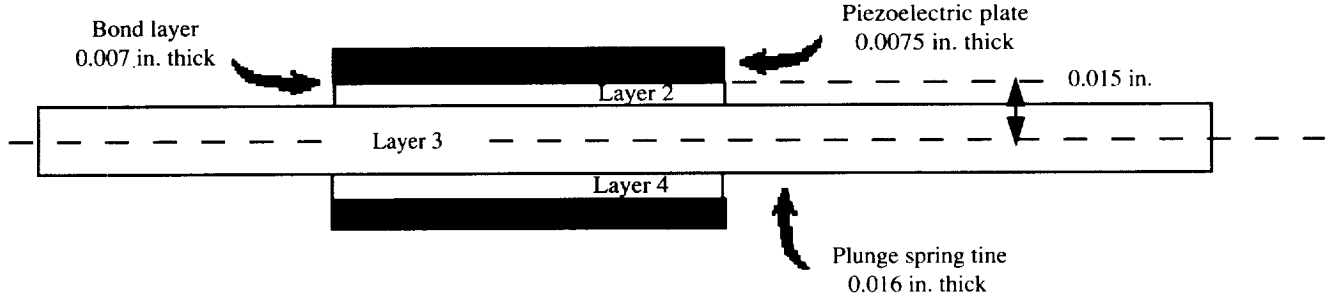
39

Figure D1. Actuator attachment.

integral over the thickness is decomposed into several parts:

$$M_{\Lambda_2} = \left(\gamma_1 \int_{\text{Layer 1}} z\,dz + \gamma_2 \int_{\text{Layer 2}} z\,dz \right.$$

$$+ \gamma_3 \int_{\text{Layer 3}} z\,dz + \gamma_4 \int_{\text{Layer 4}} z\,dz$$

$$\left. + \gamma_5 \int_{\text{Layer 5}} z\,dz \right) V_3 \qquad \text{(D14)}$$

where the layer geometry is defined in figure D1.

The constant γ is a function of the electro-mechanical coupling coefficient d_{31}. Neither the steel nor the bonding compound exhibits any coupling behavior, so for layers 2, 3, and 4, the coupling coefficients are all zero. As long as oppositely oriented voltages are applied to the top and bottom plates, the plates are geometrically and electrically similar such that the integrals through the layers are equal. Therefore,

$$M_{\Lambda_2} = 2\gamma_1 V_3 \int_{\bar{z}}^{\bar{z}+t} z\,dz \qquad \text{(D15)}$$

After solving the integral,

$$M_{\Lambda_2} = \gamma_1 V_3 \left(2\bar{z}t + t^2 \right) \qquad \text{(D16)}$$

and

$$\mathbf{F}_2 = \iint_{\text{Area}} -\frac{\partial^2 \Psi_z}{\partial y^2} \gamma_1 V_3 \left(2\bar{z}t + t^2 \right) dA \qquad \text{(D17)}$$

To implement the actuator equation, numerical integration must be performed. The integral equation is approximated as a summation over the node points of a discretized structural model (ref. 32):

$$\iint_{\text{Area}} [\ ]\,dA = \sum_{j=1}^{\text{n nodes}} [\ ]_j\, A_j \qquad \text{(D18)}$$

where A_j is the surface area associated with each node. Therefore

$$\mathbf{F}_2 = \sum_{j=1}^{\text{n nodes}} \gamma_1 \left(2\bar{z}t + t^2 \right) \left(-\frac{\partial^2 \Psi_z}{\partial y^2} \right)_j A_j V_3 \quad \text{(D19)}$$

There are two modes used in the analysis, so

$$\mathbf{F}_2 = \gamma_1 \left(2\bar{z}t + t^2 \right) \left\{ \begin{array}{c} \sum_{j=1}^{\text{n nodes}} \left(-\frac{\partial^2 \Psi_{z1}}{\partial y^2} \right)_j A_j \\ \sum_{j=1}^{\text{n nodes}} \left(-\frac{\partial^2 \Psi_{z2}}{\partial y^2} \right)_j A_j \end{array} \right\} V_3 \quad \text{(D20)}$$

$$\mathbf{F}_2 = \left\{ \begin{array}{c} \Gamma_1 \\ \Gamma_2 \end{array} \right\} d_{31} V_3 \qquad \text{(D21)}$$

where Γ_i is associated with the ith mode:

$$\Gamma_i = (2\bar{z} + t) \left(\frac{\nu_{12} + 1}{1 - \nu_{12}\nu_{21}} \right) E_2 \sum_{j=1}^{\text{n nodes}} \left(-\frac{\partial^2 \Psi_{zi}}{\partial y^2} \right)_j A_j \quad \text{(D22)}$$

Appendix E

Logarithmic Decrement Method for Determining Damping

The logarithmic decrement is defined for a decaying cyclic system by the ratio of peak magnitudes for two cycles, which are n cycles apart:

$$\delta = \frac{1}{n}\ln\left(\frac{x_1}{x_n}\right) \qquad (E1)$$

The relationship of the logarithmic decrement to the damping ratio is

$$\delta' = \frac{2\pi\zeta}{\sqrt{1-\zeta^2}} \qquad (E2)$$

which for small values of damping can be approximated

$$\delta = 2\pi\zeta \qquad (E3)$$

giving the formula for damping ratio

$$\zeta = \frac{1}{2\pi n}\ln\left(\frac{x_1}{x_n}\right) \qquad (E4)$$

Note that the structural damping g is twice the damping ratio ζ.

References

1. Sandford, Maynard C.; Abel, Irving; and Gray, David L.: *Development and Demonstration of a Flutter-Suppression System Using Active Controls.* NASA TR R-450, 1975.

2. Newsom, Jerry R.; and Abel, Irving: *Some Experiences With Active Control of Aeroelastic Response.* NASA TM-83179, 1981.

3. Newsom, Jerry R.; and Pototzky, Anthony S.: Analysis and Flight Data for a Drone Aircraft With Active Flutter Suppression. *J. Aircr.*, vol. 19, no. 11, Nov. 1982, pp. 1012–1018.

4. Waszak, Martin R.; and Srinathkumar, S.: Active Flutter Suppression: Control System Design and Experimental Validation. *A Collection of Technical Papers, Volume 1—AIAA Guidance, Navigation and Control Conference*, American Inst. of Aeronautics and Astronautics, Inc., Aug. 1991, pp. 276–286. (Available as AIAA-91-2629-CP.)

5. Hwang, C.; Winther, B. A.; and Mills, G. R.: *Demonstration of Active Wing/Store Flutter Suppression Systems.* AFFDL-TR-78-65, U.S. Air Force, June 1978. (Available from DTIC as AD B030 735L.)

6. Ehlers, Steven Michael: Aeroelastic Behavior of an Adaptive Lifting Surface. Ph.D. Thesis, Purdue Univ., Aug. 1991.

7. Anderson, Eric H.; and Crawley, Edward F.: *Piezoceramic Actuation of One- and Two-Dimensional Structures.* SSL #5-89, Dep. of Aeronautics and Astronautics, Massachusetts Inst. of Technology, May 1989.

8. Scott, Robert Charles: Control of Flutter Using Adaptive Materials. M.S. Thesis, Purdue Univ., May 1990.

9. Spangler, Ronald L., Jr.; and Hall, Steven R.: Piezoelectric Actuators for Helicopter Rotor Control. *A Collection of Technical Papers, Part 3—AIAA/ASME/ASCE/AHS/ASC 31st Structures, Structural Dynamics and Materials Conference*, American Inst. of Aeronautics and Astronautics, Inc., Apr. 1990, pp. 1589–1599. (Available as AIAA-90-1076-CP.)

10. Barrett, Roland: Intelligent Rotor Blade and Structures Development Using Directionally Attached Piezoelectric Crystals. M.S. Thesis, Univ. of Maryland, 1990.

11. Preumont, André; Dufour, Jean-Paul; and Malekian, Christian: Active Damping by a Local Force Feedback With Piezoelectric Actuators. *A Collection of Technical Papers, Part 3, Structural Dynamics I—AIAA/ASME/ASCE/AHS/ASC 32nd Structures, Structural Dynamics, and Materials Conference*, American Inst. of Aeronautics and Astronautics, Inc., Apr. 1991, pp. 1879–1887. (Available as AIAA-91-0989-CP.)

12. Lefebvre, Sylvie: Active Control of Interior Noise Using Piezoelectric Actuators in a Large-Scale Composite Fuselage Model. M.S. Thesis, Virginia Polytechnic Inst. and State Univ., June 1991.

13. Gibbs, Gary P.; and Fuller, Chris R.: Experiments on Active Control of Vibrational Power Flow Using Piezoceramic Actuators and Sensors. *A Collection of Technical Papers, Part 4—AIAA/ASME/ASCE/AHS/ASC 31st Structures, Structural Dynamics, and Materials Conference*, American Inst. of Aeronautics and Astronautics, Inc., Apr. 1990, pp. 2331–2339. (Available as AIAA-90-1132-CP.)

14. de Luis, Javier; and Crawley, Edward F.: Experimental Results of Active Control on a Prototype Intelligent Structure. *A Collection of Technical Papers, Part 4—AIAA/ASME/ASCE/AHS/ASC 31st Structures, Structural Dynamics and Materials Conference*, American Inst. of Aeronautics and Astronautics, Inc., Apr. 1990, pp. 2340–2350. (Available as AIAA-90-1163-CP.)

15. Weisshaar, Terrence A.; and Ehlers, Steven M.: Adaptive Static and Dynamic Aeroelastic Design. Purdue University and McDonnell-Douglas Technologies, Inc., paper presented at the 1991 International Forum on Aeroelasticity and Structural Dynamics Workshop on Smart Material Systems and Structures (Aachen, Germany), June 6, 1991.

16. Ehlers, S. M.; and Weisshaar, T. A.: Static Aeroelastic Behavior of an Adaptive Laminated Piezoelectric Composite Wing. *A Collection of Technical Papers, Part 3—AIAA/ASME/ASCE/AHS/ASC 31st Structures, Structural Dynamics and Materials Conference*, American Inst. of Aeronautics and Astronautics, Inc., Apr. 1990, pp. 1611–1623. (Available as AIAA-90-1078-CP.)

17. Lazarus, Kenneth B.; Crawley, Edward F.; and Lin, Charrissa Y.: Fundamental Mechanisms of Aeroelastic Control With Control Surface and Strain Actuation. *A Collection of Technical Papers, Part 3, Structural Dynamics I—AIAA/ASME/ASCE/AHS/ASC 32nd Structures, Structural Dynamics, and Materials Conference*, American Inst. of Aeronautics and Astronautics, Inc., Apr. 1991, pp. 1817–1831. (Available as AIAA-91-0985-CP.)

18. Mason, Warren P.: Piezoelectricity, Its History and Applications. *J. Acoust. Soc. America*, vol. 70, no. 6, Dec. 1981, pp. 1561–1566.

19. Dunn, H. J.: Experimental Results of Active Control on a Large Structure To Suppress Vibration. *A Collection of Technical Papers, Volume 2—AIAA Guidance, Navigation, and Control Conference*, American Inst. of Aeronautics and Astronautics, Inc., Aug. 1991, pp. 779–791. (Available as AIAA-91-2692-CP.)

20. *MSC/NASTRAN User's Manual—MSC/NASTRAN Version 65.* MSR-39, MacNeal-Schwendler Corp., Nov. 1985.

21. Roark, Raymond J.; and Young, Warren C.: *Formulas for Stress and Strain*, Fifth ed. McGraw-Hill Book Co., c.1975.

22. Rodden, W. P.; Giesing, J. P.; and Kálmán, T. P.: New Developments and Applications of the Subsonic Doublet-Lattice Method for Nonplanar Configurations. *Symposium on Unsteady Aerodynamics for Aeroelastic Analyses of Interfering Surfaces*, AGARD-CP-80, Apr. 1971, pp. 4-1–4-27.

23. Tiffany, Sherwood H.; and Adams, William M., Jr.: *Nonlinear Programming Extensions to Rational Function Approximation Methods for Unsteady Aerodynamic Forces.* NASA TP-2776, 1988.

24. Hoadley, Sherwood Tiffany; Adams, William M., Jr.; and Silva Walter A.: *ISACv5.1—Interaction Structures, Aerodynamics, and Controls. Version 5.1 User's Manual With Guides for VMS or UNIX Operating Systems.* NASA TM-100666, 1992.

25. Longman, Richard W.; Juang, Jer-Nan; and Phan, Minh: *Input and Output Matrices in Modal Identification.* NASA TM-107633, 1992.

26. *MATRIX$_x$ 7.0 Release Notes.* Integrated Systems Inc., Oct. 1988.

27. *MATLAB^{TM} for Macintosh Computers.* MathWorks, Inc., Apr. 4, 1989.

28. Kuo, Benjamin C.: *Digital Control Systems.* Holt, Rinehart and Winston Inc., c.1980.

29. Adams, William M., Jr.; Tiffany, Sherwood H.; Newsom, Jerry R.; and Peele, Ellwood L.: *STABCAR—A Program for Finding Characteristic Roots of Systems Having Transcendental Stability Matrices.* NASA TP-2165, 1984.

30. Franklin, Gene F.; Powell, J. David; and Emani-Naeini, Abbas: *Feedback Control of Dynamic Systems.* Addison-Wesley Publ. Co., 1986.

31. Phillips, Charles L.; and Nagle, H. Troy, Jr.: *Digital Control System Analysis and Design.* Prentice-Hall, Inc., c.1984.

32. Kohn, Michael C.: *Practical Numerical Methods.* Macmillan Publ. Co., Inc., c.1987.

33. Yates, E. Carson, Jr.: Flutter and Unsteady-Lift Theory. *Performance and Dynamics of Aerospace Vehicles,* NASA SP-258, 1971, pp. 289–374.

34. Mukhopadhyay, Vivek; Newsom, Jerry R.; and Abel, Irving: *A Method for Obtaining Reduced-Order Control Laws for High-Order Systems Using Optimization Techniques.* NASA TP-1876, 1981.

35. Chia, Chuen-Yuan: *Nonlinear Analysis of Plates.* McGraw-Hill, Inc., c.1980.

REPORT DOCUMENTATION PAGE

Form Approved
OMB No. 0704-0188

1. AGENCY USE ONLY *(Leave blank)*	2. REPORT DATE March 1993	3. REPORT TYPE AND DATES COVERED Technical Paper

4. TITLE AND SUBTITLE

Analytical and Experimental Investigation of Flutter Suppression by Piezoelectric Actuation

5. FUNDING NUMBERS

WU 505-63-50-15

6. AUTHOR(S)

Jennifer Heeg

7. PERFORMING ORGANIZATION NAME(S) AND ADDRESS(ES)

NASA Langley Research Center
Hampton, VA 23681-0001

8. PERFORMING ORGANIZATION REPORT NUMBER

L-17024

9. SPONSORING/MONITORING AGENCY NAME(S) AND ADDRESS(ES)

National Aeronautics and Space Administration
Washington, DC 20546-0001

10. SPONSORING/MONITORING AGENCY REPORT NUMBER

NASA TP-3241

11. SUPPLEMENTARY NOTES

12a. DISTRIBUTION/AVAILABILITY STATEMENT

Unclassified–Unlimited

Subject Category 05

12b. DISTRIBUTION CODE

13. ABSTRACT *(Maximum 200 words)*

The objective of this research was to analytically and experimentally study the capabilities of piezoelectric plate actuators for suppressing flutter. Piezoelectric materials are characterized by their ability to produce voltage when subjected to a mechanical strain. The converse piezoelectric effect can be utilized to actuate a structure by applying a voltage. For this investigation, a two-degree-of-freedom wind tunnel model was designed, analyzed, and tested. The model consisted of a rigid wing and a flexible mount system that permitted a translational and a rotational degree of freedom. The model was designed such that flutter was encountered within the testing envelope of the wind tunnel. Actuators made of piezoelectric material were affixed to leaf springs of the mount system. Command signals, applied to the piezoelectric actuators, exerted control over the damping and stiffness properties. A mathematical aeroservoelastic model was constructed by using finite element methods, laminated plate theory, and aeroelastic analysis tools. Plant characteristics were determined from this model and verified by open loop experimental tests. A flutter suppression control law was designed and implemented on a digital control computer. Closed loop flutter testing was conducted. The experimental results represent the first time that adaptive materials have been used to actively suppress flutter. They demonstrate that small, carefully placed actuating plates can be used effectively to control aeroelastic response.

14. SUBJECT TERMS Piezoelectric actuation; Flutter suppression; Aeroservoelasticity; Active controls; Adaptive structures	15. NUMBER OF PAGES 46
	16. PRICE CODE A03

17. SECURITY CLASSIFICATION OF REPORT Unclassified	18. SECURITY CLASSIFICATION OF THIS PAGE Unclassified	19. SECURITY CLASSIFICATION OF ABSTRACT	20. LIMITATION OF ABSTRACT

NSN 7540-01-280-5500

Standard Form 298(Rev. 2-89)
Prescribed by ANSI Std. Z39-18
298-102

NASA-Langley, 1993